

**Supplementary Information for 'Frustrated charge density wave and quasi-long-range bond-orientational order in the magnetic kagome FeGe'**

**CONTENTS**

S1. Sample growth and characterization	2
S2. x-ray diffraction	2
S3. Angle Resolved Photoemission: ARPES	4
S4. First-principle calculation methods	6
S5. Bulk band structure in non-CDW and CDW phases	6
S6. Surface band structure in the CDW phase	6
S7. Diffuse scattering, DS	13
A. FeGe	15
B. Annealed FeGe	15
C. FeGe <sub>0.9</sub>	17
D. FeSn	20
S8. Monte Carlo simulation of DS	21
A. Ising model for Ge dimerization	21
B. Monte Carlo simulation	21
S9. Bond-order correlation function analysis	24
References	27

## S1. SAMPLE GROWTH AND CHARACTERIZATION

Single crystals of FeGe were grown by the chemical vapor transport method (see Methods) and characterized by means of energy dispersion x-ray (EDX) analysis, Laue diffraction, resistivity and magnetization (figure S1).

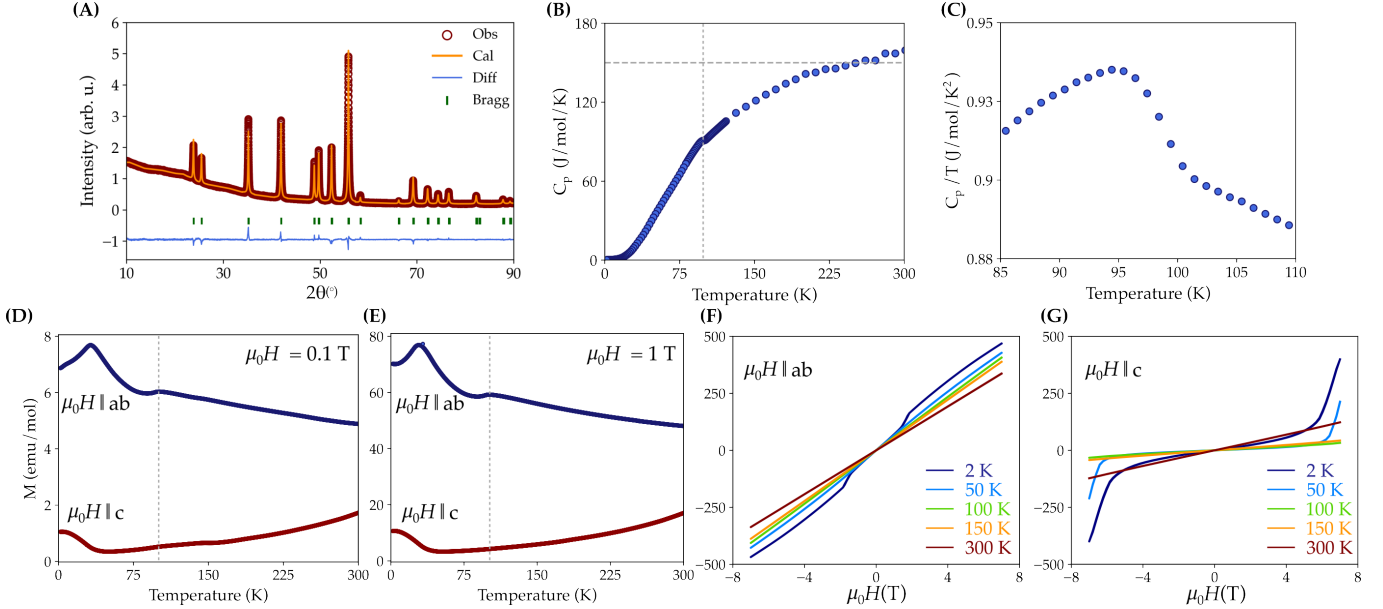


FIG. S1. Characterization of FeGe. (A) Powder x-ray diffraction refinement and its LeBail refinement. (B) Temperature dependence of the heat capacity. (C) Heat capacity divided by temperature, highlighting the CDW phase transition. (D-E) Temperature dependence of the magnetization for applied magnetic fields of 0.1 T and 1 T, respectively. (F-G) Magnetization versus magnetic field parallel (F) and perpendicular (G) to the kagome plane.

Figure S1 (A) shows the LeBail refinement of grounded FeGe single crystals. No impurity phases were observed, specially the presence of the cubic B20 phase. Both the specific heat ( $C_p$ ), figure S1 (B-C) and the magnetization, figure S1 (D-E), identify the CDW transition at  $\sim 105$ K. The transport properties are in nice agreement with the reports in the literature [1, 2].

## S2. X-RAY DIFFRACTION

This section contains the single crystal structural refinement of FeGe at 80 K. Both  $P6mm$  (non-centrosymmetric), Table S1, and  $P6mm$  (centrosymmetric) Table S2 could be equally indexed with similar *Goodness-of-Fit*. The x-ray refinements were carried out with SHELXL2018/1 code (see Methods).

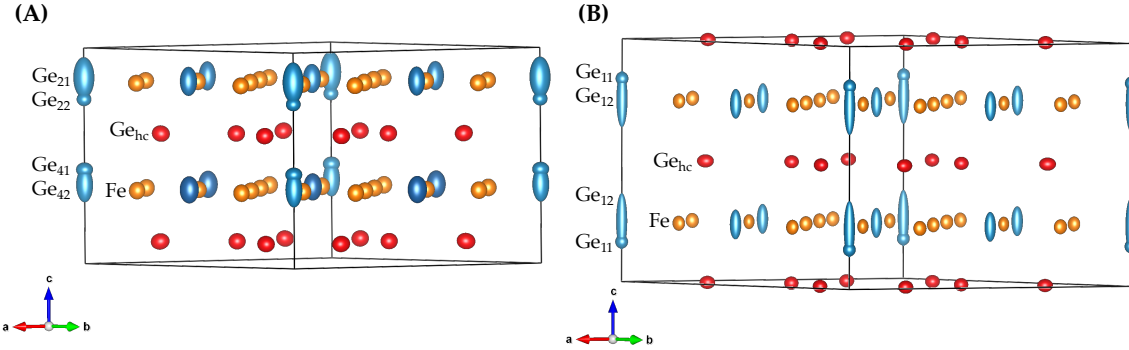


FIG. S2. (A) CDW unit cell of the space group 183 and (B) space group 191.

Figure S2 displays the low temperature CDW unit cell within the space group 183 (non-centrosymmetric  $P6mm$ ) and 191 (centrosymmetric  $P6mmm$ ). The dimerized trigonal Ge in the space group 183 creates 4 in-equivalent trigonal Ge in the kagome

plane ( $\text{Ge}_{21}$ ,  $\text{Ge}_{22}$ ,  $\text{Ge}_{41}$  and  $\text{Ge}_{42}$ ), while the dimerization on the space group 191 splits the trigonal Ge into 2  $\text{Ge}_{11}$  and  $\text{Ge}_{21}$ .

TABLE S1. Crystal data and structure refinement for 80 K:  $P6mm$  symmetry, space group n°= 183. Unit cell dimensions  $a = b = 9.97740(2)$  Å,  $c = 8.10070(10)$  Å,  $\alpha=\beta= 90^\circ$ ,  $\gamma = 120^\circ$ . Volume =698.3738(20) Å<sup>3</sup>.  $R_1=0.056$

		<i>x</i>	<i>y</i>	<i>z</i>	Occ.	<i>U</i>	Site	Sym.
Ge	$\text{Ge}_1$	0.33333	0.66667	0.60251	1.000	0.012	2b	3m.
Ge	$\text{Ge}_{22}$	1.00000	1.00000	0.76210	0.309	0.009	1a	6mm
Ge	$\text{Ge}_{21}$	1.00000	1.00000	0.86285	0.691	0.036	1a	6mm
Ge	$\text{Ge}_3$	0.67051	0.83526	0.10257	1.000	0.013	6e	.m.
Ge	$\text{Ge}_{41}$	1.00000	1.00000	0.43604	0.378	0.011	1a	6mm
Ge	$\text{Ge}_{42}$	1.00000	1.00000	0.36518	0.622	0.025	1a	6mm
Ge	$\text{Ge}_5$	0.66412	0.83206	0.60263	1.000	0.013	6e	.m.
Ge	$\text{Ge}_6$	0.33333	0.66667	0.10276	1.000	0.012	2b	3m.
Ge	$\text{Ge}_7$	0.50000	1.00000	0.85698	1.000	0.020	3c	2mm
Ge	$\text{Ge}_8$	0.50000	1.00000	0.35434	1.000	0.020	3c	2mm
Fe	$\text{Fe}_1$	0.74954	1.00000	0.34468	1.000	0.012	6d	.m.
Fe	$\text{Fe}_2$	0.50020	0.75010	0.84475	1.000	0.012	6e	.m.
Fe	$\text{Fe}_3$	0.49999	0.75000	0.34241	1.000	0.012	6e	.m.
Fe	$\text{Fe}_4$	0.74963	1.00000	0.84234	1.000	0.012	6d	.m.

TABLE S2. Crystal data and structure refinement for 80 K:  $P6/mmm$  symmetry, space group n°= 191. Unit cell dimensions  $a = 9.97750(10)=b = 9.97750(10)$  Å,  $c = 8.10030(10)$  Å,  $\alpha=\beta= 90^\circ$ ,  $\gamma = 120^\circ$ . Volume =698.353(16) Å<sup>3</sup>,  $R_1=0.056$

		<i>x</i>	<i>y</i>	<i>z</i>	Occ.	<i>U</i>	Site	Sym.
Fe	$\text{Fe}_1$	0.25053	0.00000	0.75162	1.000	0.004	12n	.m
Fe	$\text{Fe}_2$	0.24996	0.49991	0.74843	1.000	0.004	12o	.m.
Ge	$\text{Ge}_{11}$	0.00000	0.00000	0.83590	0.485	0.004	2e	6mm
Ge	$\text{Ge}_{12}$	0.00000	0.00000	0.75170	0.515	0.028	2e	6mm
Ge	$\text{Ge}_2$	0.50000	0.00000	0.74842	1.000	0.009	6i	2mm
Ge	$\text{Ge}_3$	0.16844	0.33687	0.00000	1.000	0.005	6l	mm2
Ge	$\text{Ge}_4$	0.83593	0.67186	0.50000	1.000	0.005	6m	mm2
Ge	$\text{Ge}_5$	0.33333	0.66667	0.00000	1.000	0.005	2c	-6m2
Ge	$\text{Ge}_6$	0.66667	0.33333	0.50000	1.000	0.005	2d	-6m2

### S3. ANGLE RESOLVED PHOTOEMISSION: ARPES

We observe the following key features in the experimental band structure from ARPES:

1. A clear Dirac crossing appears at  $K$  at about -0.65 eV.
2. A V-shaped band centered at  $\Gamma$  with the bottom at about -1.0 eV.
3. A very broad spectrum weight connects  $\Gamma$  and the Dirac crossing at  $K$ , which could be the weights from the Dirac bands and together with other bands.
4. A U-shaped band centered at  $\Gamma$  with the bottom at about -0.28 eV.

The first two features in APRES, i.e., the Dirac crossing at  $K$  and the V-shaped band at  $\Gamma$  could be well-matched using the CDW bulk band structure in DFT, as shown in figure S3. The broad spectrum weight connects  $\Gamma$  and at  $K$  is also seen in DFT, although the energy in DFT is slightly higher. However, the U-shape is not seen in the bulk bands. We argue that it can be matched using the surface bands in the honeycomb Ge termination, as shown in S3.

Besides the aforementioned features that have a good matching between DFT bands and ARPES, we also observe some features that cannot be well matched. They include: (i) In DFT, there exists another Dirac-like crossing at  $K$  at about -0.4 eV, which is not seen in the APRES. (ii) The broad weight at -1 eV near  $\Gamma$  in DFT is also not seen in the ARPES. (iii) In the folded surface bands, there exist many other bands that could not have a good match with the APRES, probably due to the inaccurate description of surface instructions in DFT.

We conclude that the main features in the experimental ARPES bands could be well-matched by DFT. However, since the system has a large number of bands near the Fermi level, it shows a heavily broadened spectrum where the discrepancy in the detailed features between theory and experiments is expected.

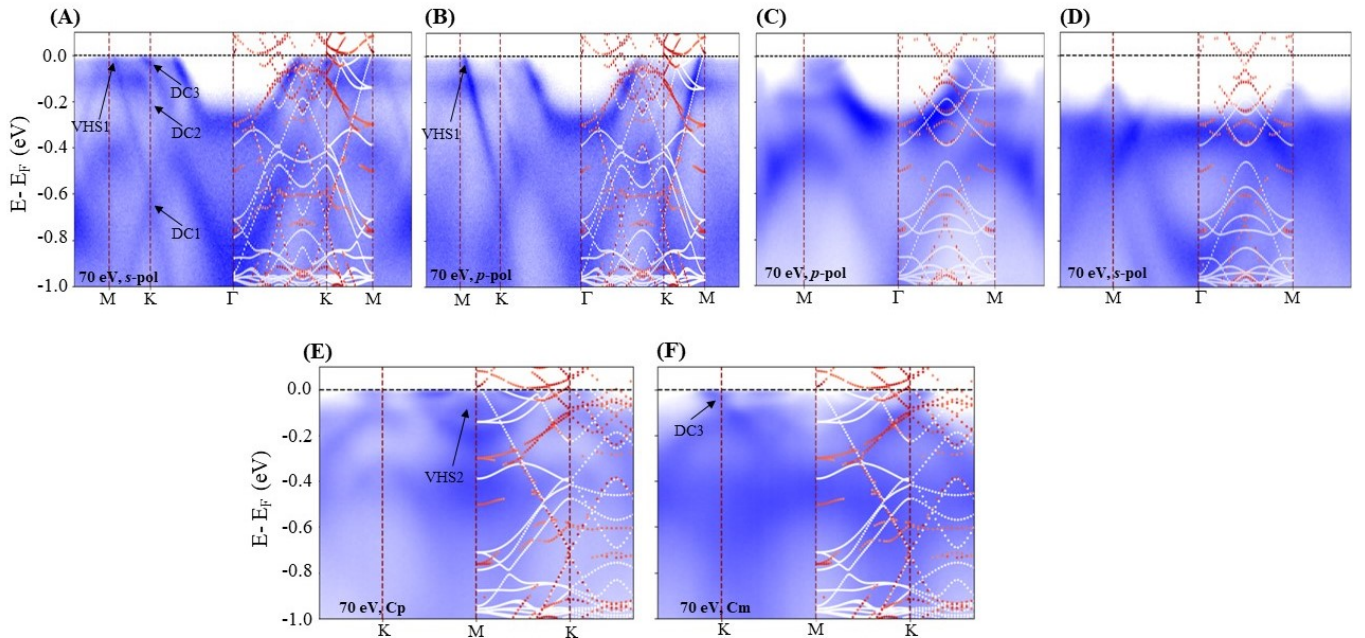


FIG. S3. A comparison between ARPES and DFT calculated energy dispersion spectra. Valance band electronic structure of FeGe obtained with 70 eV incident photon energy along (A)-(B)  $M - K - \Gamma - K - M$  symmetry direction with  $s$ -pol and  $p$ -polarized incident light, respectively. (C)-(D) along  $M - \Gamma - M$  symmetry direction with  $p$ -pol and  $s$ -polarized light, respectively. (E)-(F) Along  $K - M - K$  symmetry direction with circular positive ( $C_p$ ) and circular negative ( $C_m$ ) incident light, respectively. ('DC' and 'VHS' represent the Dirac cone, and Van Hove singularity, respectively). On top of the VB spectra, DFT calculated bulk folded band structure in the CDW phase (white) and Ge terminated surface band structure (red) are overlapped.

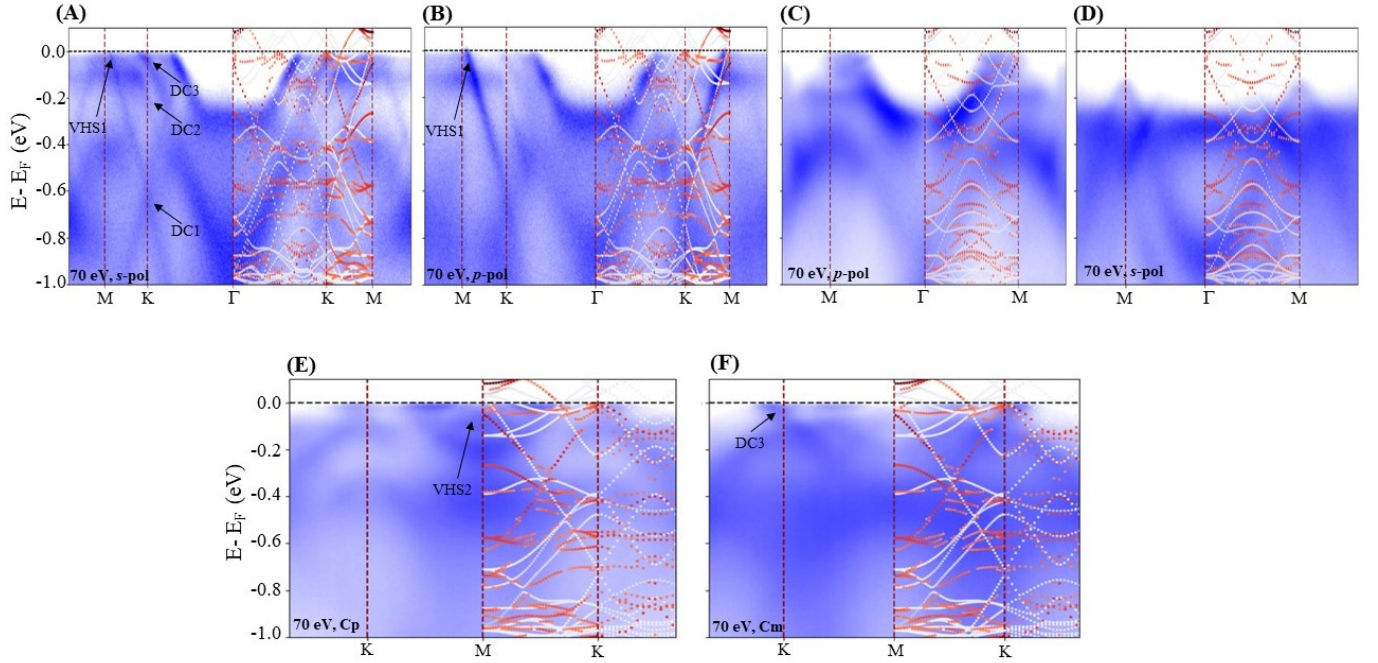


FIG. S4. A comparison between ARPES and DFT calculated spectra. The valence band specters of FeGe were obtained with 70 eV incident photon energy along (A)-(B)  $M - K - \Gamma - K - M$  symmetry direction with  $s$ -pol and  $p$ -polarized incident light, respectively. (C)-(D) along  $M - \Gamma - M$  symmetry direction with  $p$ -pol and  $s$ -polarized light, respectively. (E)-(F) Along  $K - M - K$  symmetry direction with circular positive ( $C_p$ ) and circular negative ( $C_m$ ) incident light, respectively. ('DC' and 'VHS' represent the Dirac cone, and Van Hove singularity, respectively). Here, the 'white' bands are folded bulk bands of FeGe calculated in CDW phase where as the 'red' ones are the unfolded surface bands obtained with Kagome termination.

#### S4. FIRST-PRINCIPLE CALCULATION METHODS

The first-principle calculations in this work use the Vienna ab-initio Simulation Package (VASP)[3–7] with generalized gradient approximation of Perdew-Burke-Ernzerhof (PBE) exchange-correlation potential[8]. A  $8 \times 8 \times 8$  ( $5 \times 5 \times 5$ )  $k$ -mesh for non-CDW (CDW) phase and an energy cutoff of 500 eV are used. The maximally localized Wannier functions are obtained using WANNIER90[9–12]. A local coordinate system at the kagome site is adopted in order to decompose  $d$  orbitals when construct MLWFs, the same as the one used in Ref.[13]. The Wannier tight-binding models are symmetrized using *Wannhr\_symm* in *WannierTools*[14]. The unfolding of CDW bands is performed using *VaspBandUnfolding* package[15, 16]. The Fermi surface is computed using *WannierTools*[14] and visualized using *Fermisurfer*[17].

#### S5. BULK BAND STRUCTURE IN NON-CDW AND CDW PHASES

In this section, we discuss the bulk band structure in both non-CDW and CDW phases.

In Fig. S5(a), the crystal structure of FeGe in the non-CDW phase is shown together with two surface terminations, i.e., kagome and honeycomb surfaces. In the  $2 \times 2 \times 1$  CDW phase, the main atomic displacements come from the dimerization of the triangular Ge. Experimentally, the dimerized Ge atoms have two possible positions as shown in the main text. In DFT, we fix the Ge atoms at the larger dimerized positions.

In Fig. S5(b)(c), we show the comparison between the non-CDW and (unfolded) CDW bands in the PM and AFM phases. In Fig. S8 and Fig. S9, the orbital weights in the non-CDW AFM phase are shown, while in Fig. S10, the orbital weights in the CDW phase are shown. We observe the following features in the CDW bulk bands:

- A Dirac crossing at  $K$  centered at about -0.7 eV mainly comes from  $d_{xy}$  orbitals, together with some  $d_{x^2-y^2}$  weights. It exists in both CDW and non-CDW bands and has little changes, as shown in Fig. S9(a)(b) and Fig. S10(b).
- A V-shaped band centered at  $\Gamma$  from about -0.5 to -1.0 eV mainly comes from the triangular Ge  $p_z$  orbital, as shown in Fig. S10(d). This band accounts for the main reconstruction by CDW. In the non-CDW phase, it is located at high energy with the bottom at about -0.5 eV, as shown in Fig. S9(f).
- A quasi-flat bands at about -1 eV near  $\Gamma$  mainly comes from  $d_{z^2}$  orbital, as shown in Fig. S9(c) and Fig. S10(a).

In Fig. S11, we also superimpose the CDW bulk bands with non-CDW bands for better comparison.

In Fig. S6, we show the Fermi surface (FS) of FeGe in the non-CDW AFM phase. It can be seen that there is quasi-2D FS with a weak  $k_z$ -dispersion in Fig. S6(c), which is mainly contributed by the  $d_{x^2-y^2}$ ,  $d_{xy}$  orbitals of Fe (see Fig. S8). In Fig. S7, we show the 2D slices of the FS on difference  $k_z$  planes. On the  $k_z = 0$  plane, the smallest circular FS around  $\Gamma$  is mainly given by the  $p_z$  orbitals of the triangular Ge (see Fig. S8(f)). In the CDW phase, this band moves down and is far from  $E_f$  (see Fig. S10(d)). However, there are some other bands close to  $E_f$  near  $\Gamma$  in the CDW phase, which could contribute to the FSs (see Fig. S11).

In Fig. S12, we show the nesting function ( $\text{Im-}\chi$ ) and total susceptibility ( $\text{Re-}\chi$ ) of FeGe in the AFM phase (non-CDW). In the nesting function, the dominant peak appears at the  $K$  point. In the total susceptibility, however, a broad peak appears along the boundary of the first BZ, with the highest point near  $K$ . Thus we conclude that the FS nesting cannot directly account for the CDW at  $M$  point.

#### S6. SURFACE BAND STRUCTURE IN THE CDW PHASE

In this section, we discuss the surface bands in the CDW phase. In Fig. S13, the folded surface bands for both honeycomb and kagome terminations are given, together with orbital weights. In Fig. S14, we also give the unfolded surface bands. Here the folded bands denote the bands in the CDW BZ, while unfolded bands denote those in the non-CDW BZ.

We observe the major difference between folded and unfolded surface bands is a U-shaped band centered at  $\Gamma$  at about -0.3 eV at the honeycomb surface. This U-shaped band only appears in the folded bands, which mainly comes from  $(d_{xz}, d_{yz})$  of Fe. Since this band is not seen in the unfolded bands near  $\Gamma$ , it is folded from the  $M$  point due to the  $2 \times 2$  CDW order. In the CDW bulk bands, there exist bands with a similar shape from  $(d_{xz}, d_{yz})$  near  $L = (\frac{1}{2}, 0, \frac{1}{2})$ , as shown in Fig. S10(g). Thus this surface U-shaped band can be seen as  $k_z$ -projected bulk bands with surface reconstructions.

This U-shaped band matches well with APRES results. We conjecture that there are strong disorder effects near the surface that break the translational symmetry. Thus the observed bands in ARPES can be explained by the folded surface bands.

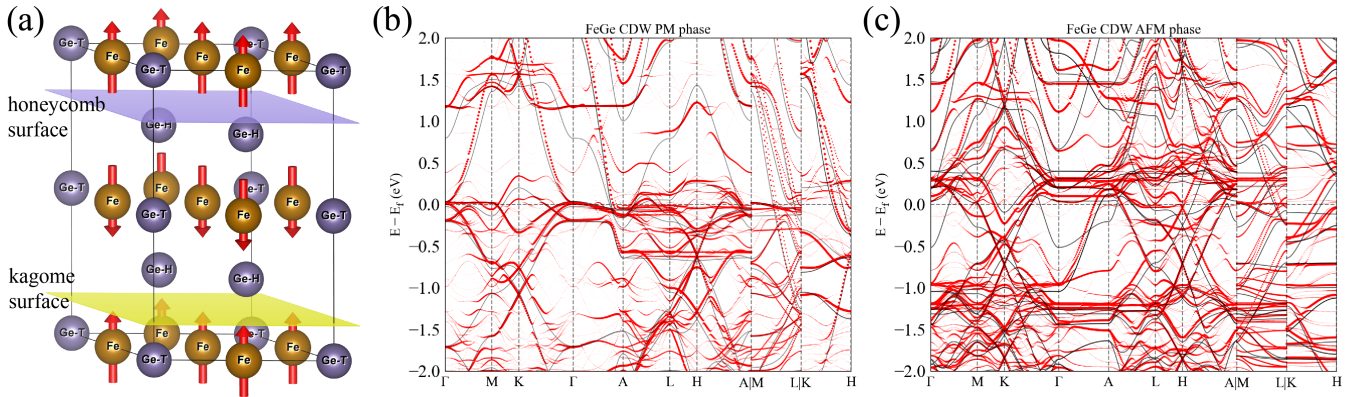


FIG. S5. (a) The crystal structure of FeGe in the non-CDW phase, where Fe atoms form kagome lattices, while Ge atoms form triangular and honeycomb lattices (denoted as Ge-T and Ge-H, respectively). Two surface terminations, i.e., kagome and honeycomb surfaces are also marked, where the atoms below the plane define the surface. (b) The band structures in non-CDW (black lines) and CDW (red lines) phases, where paramagnetic (PM) order is assumed. In the CDW phase, the bands are unfolded to the non-CDW Brillouin zone (BZ). (c) Same as (b), but in the anti-ferromagnetic (AFM) phase. Spin-orbital coupling (SOC) is neglected for simplicity as SOC is weak in FeGe.

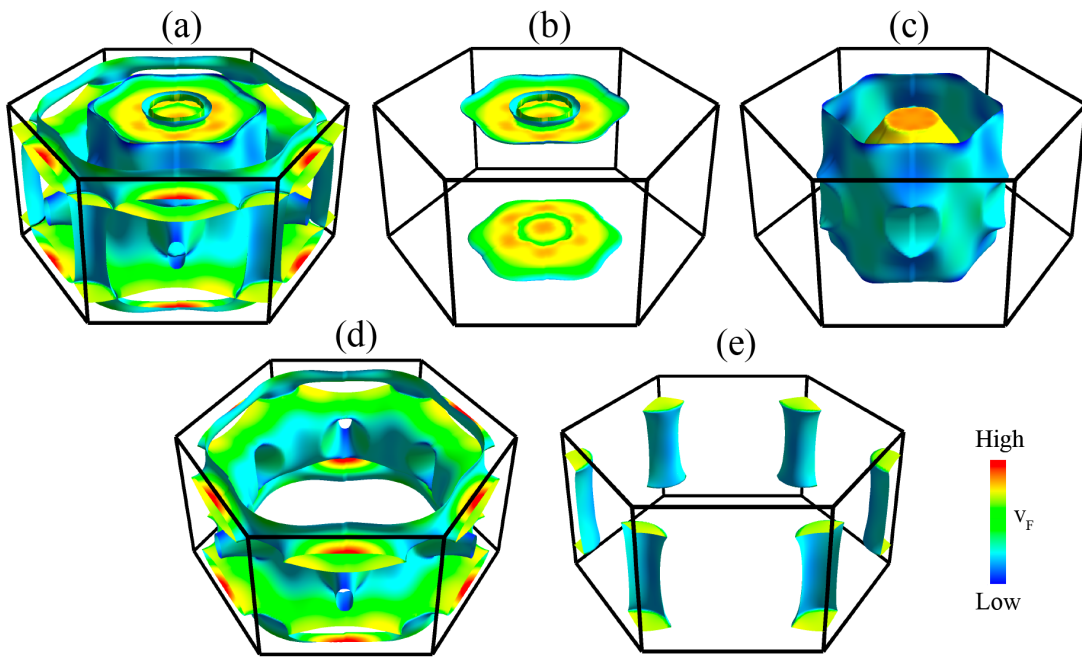


FIG. S6. The Fermi surface (FS) of FeGe in the non-CDW AFM phase, where (a) is the full FS, and (b)-(e) are four parts of FSs contributed by different bands. The color on the FS denotes the Fermi velocity. A quasi-2D FS is shown in (c) with a weak  $k_z$ -dispersion.

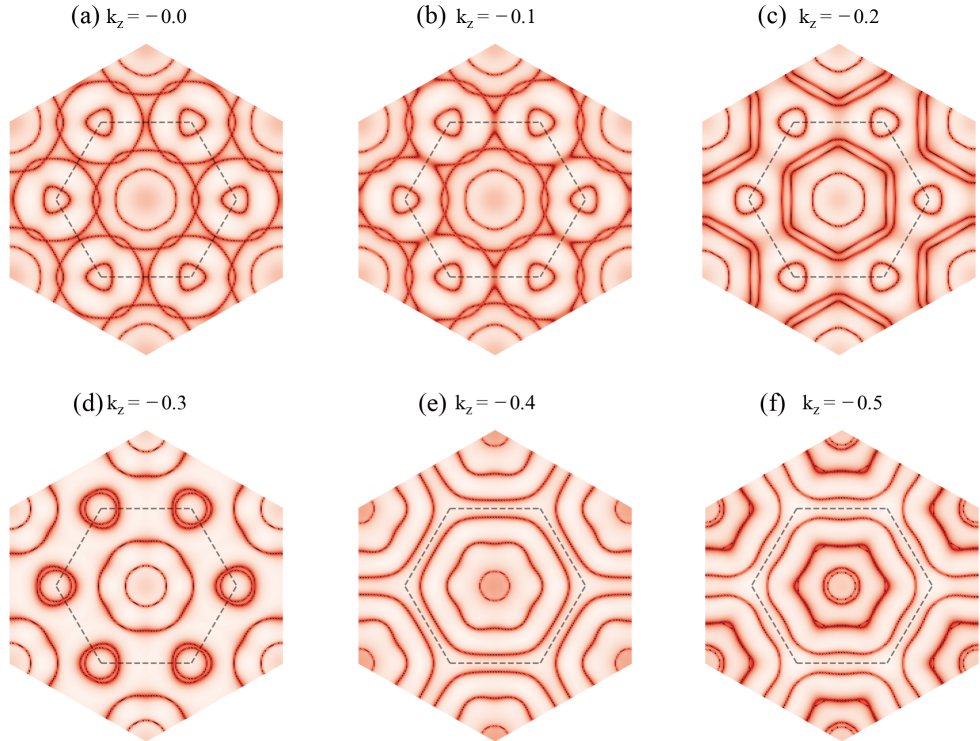


FIG. S7. The 2D Fermi surface (FS) of FeGe in the non-CDW AFM phase on different  $k_z$  planes.

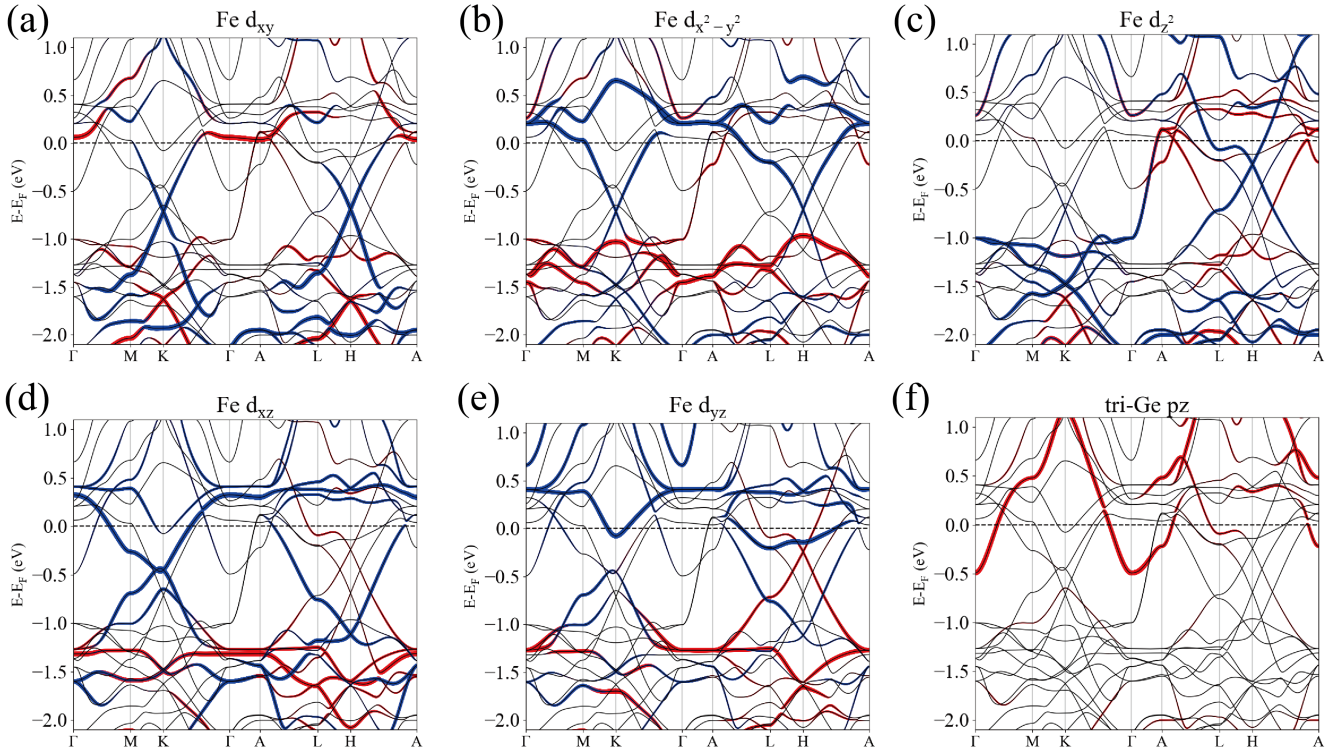


FIG. S8. The orbital projections in the non-CDW AFM phase, for Fe (a)  $d_{xy}$ , (b)  $d_{x^2-y^2}$ , (c)  $d_{z^2}$ , (d)  $d_{xz}$ , (e)  $d_{yz}$ , and triangular Ge  $p_z$  orbitals, respectively. Blue and red lines denote two spin-up and down bands from Fe one kagome layer.

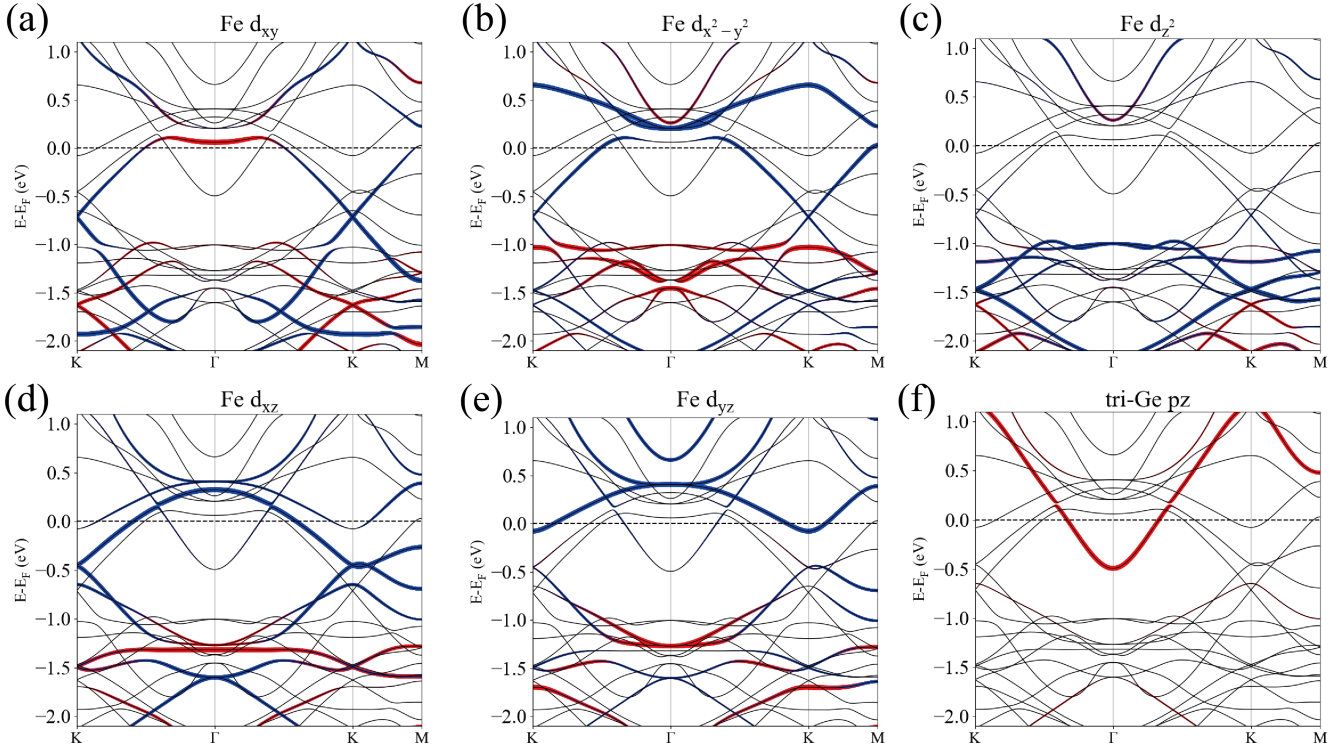


FIG. S9. The orbital projections in the non-CDW AFM phase. It is the same as Fig. S8 but on a different path in the BZ, in order to give a direct comparison with ARPES results.

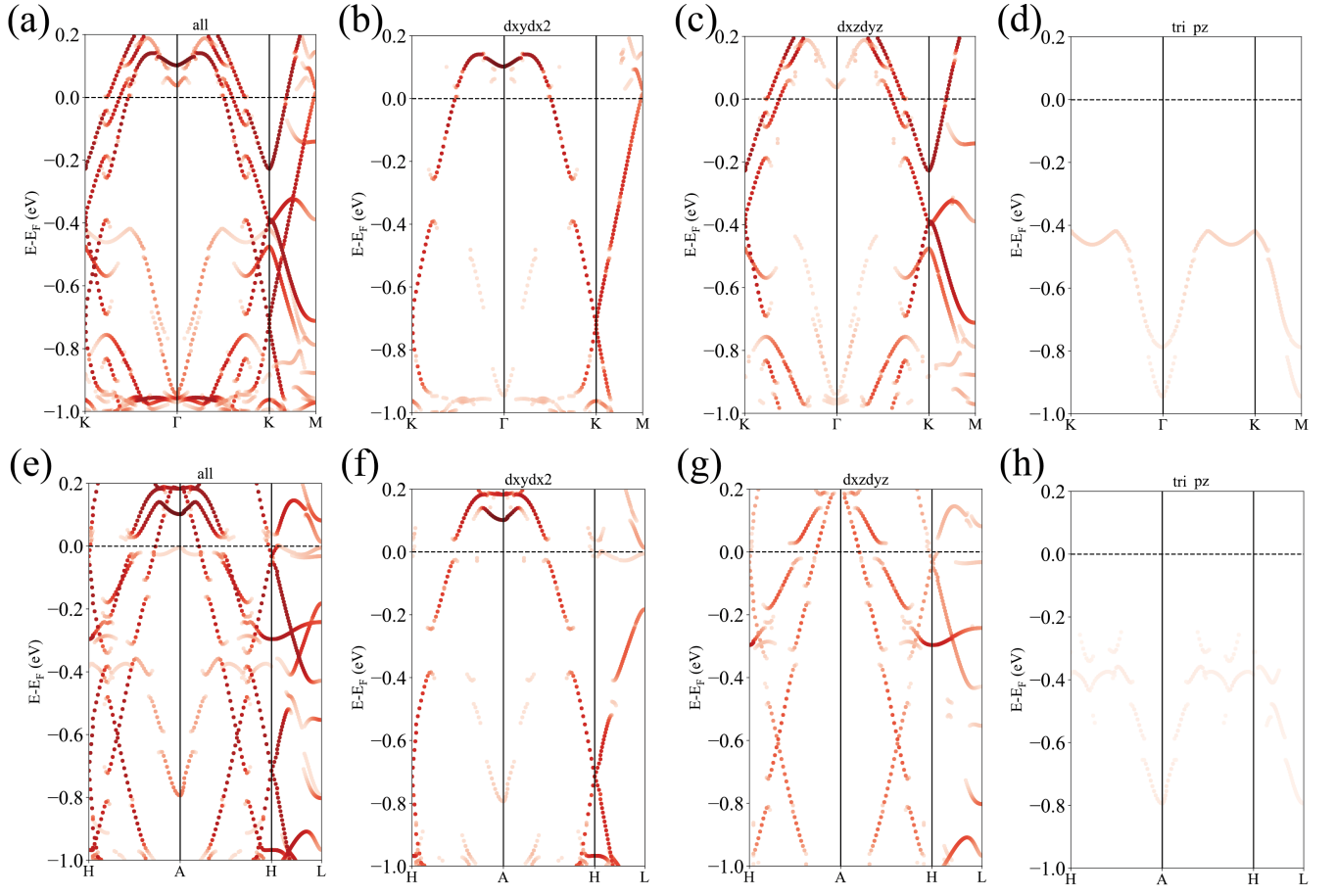


FIG. S10. The unfolded bulk band structures and orbital projections in the CDW AFM phase. (a) The unfolded bulk bands. (b)-(d) The orbital weights for Fe ( $d_{xy}, d_{x^2-y^2}$ ), ( $d_{xz}, d_{yz}$ ), and triangular Ge  $p_z$  orbitals, respectively. (e)-(h) in the second row is the same as the first row but on  $k_z = \pi$  plane.

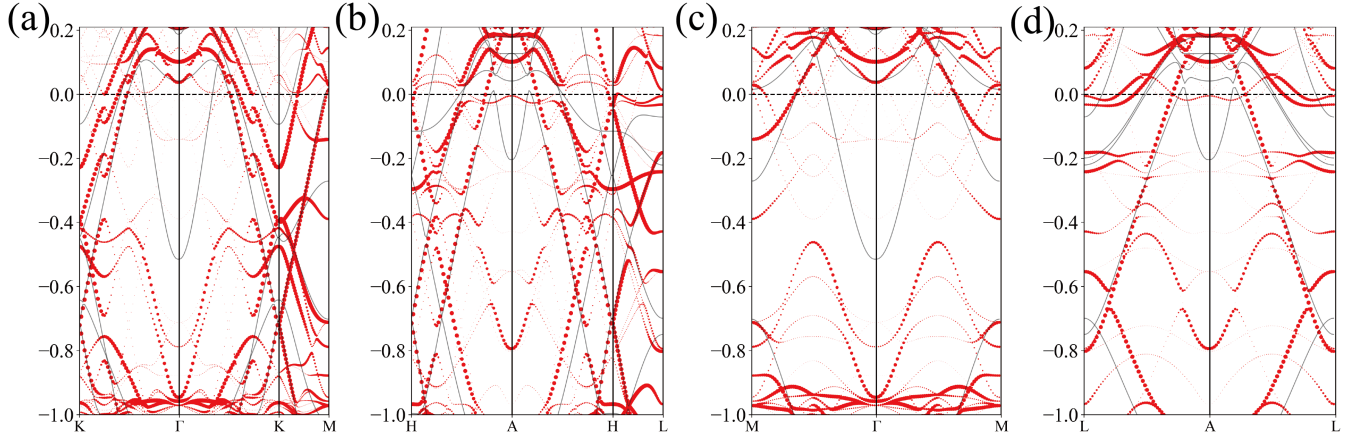


FIG. S11. Comparsion of non-CDW (black) and unfolded CDW (red) bulk bands in the AFM phase, along four different paths in the BZ. The main difference between CDW and non-CDW bands is the V-shaped bands at  $\Gamma$ , which is mainly from triangular Ge  $p_z$  orbitals (see Fig. S9 and Fig. S10 for orbital weights). This band moves down in the CDW phase.

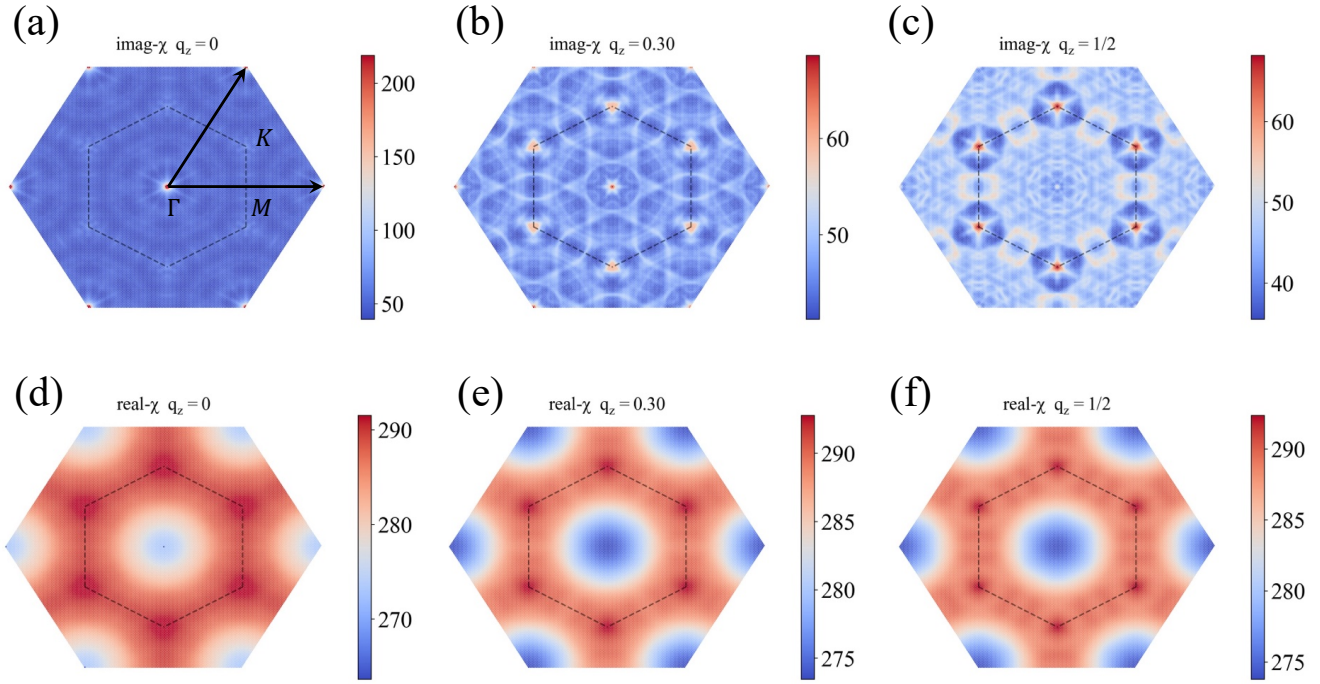


FIG. S12. The nesting function ( $\text{Im-}\chi$ ) and total susceptibility ( $\text{Re-}\chi$ ) of FeGe in the AFM phase (non-CDW). In the nesting function, the dominant peak appears at the  $K$  point. In the total susceptibility, however, a broad peak appears along the boundary of the first BZ, with the highest point near  $K$ .

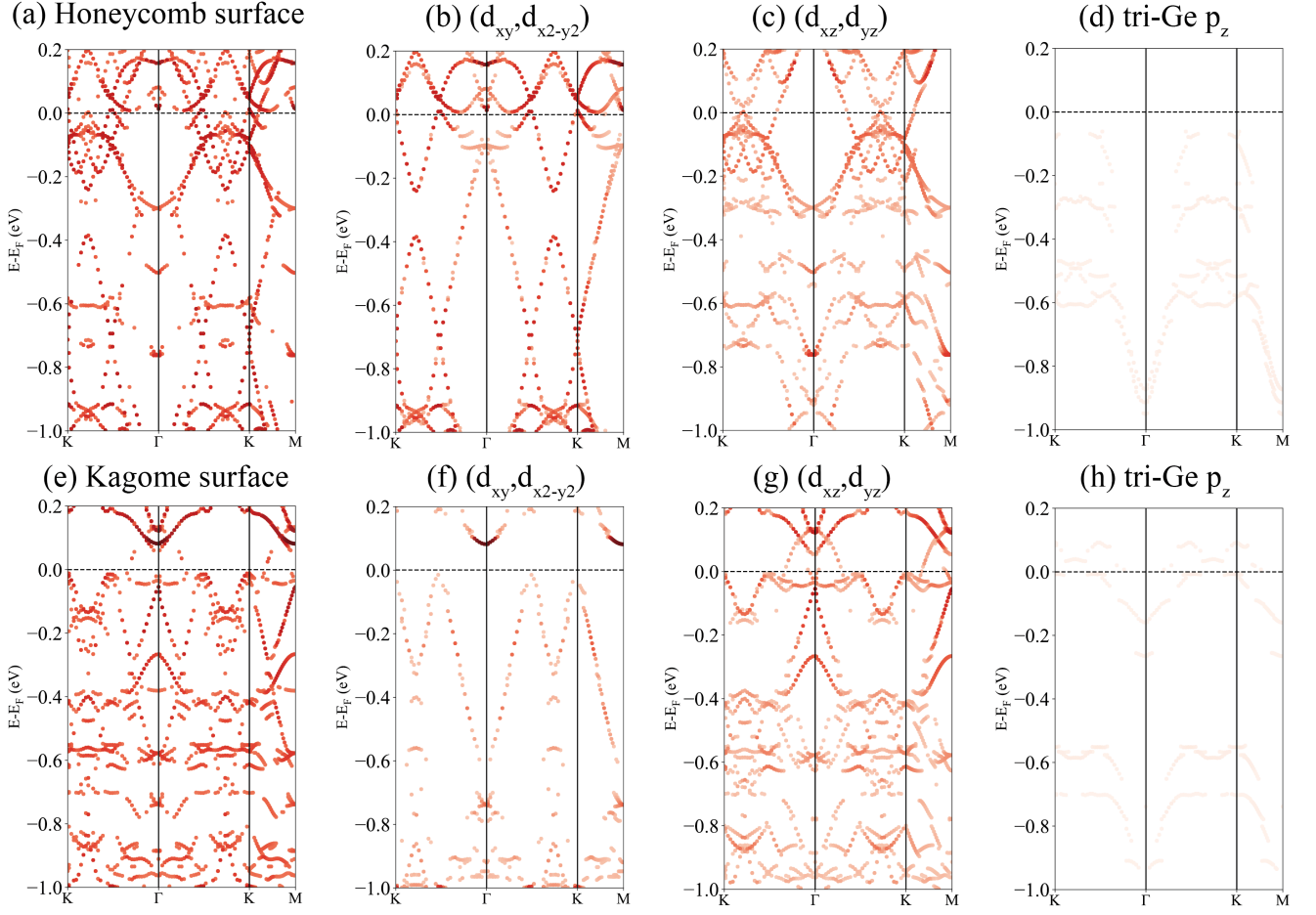


FIG. S13. The folded surface bands in the CDW phase. (a) The honeycomb surface bands. (b)-(d) The orbital weights in the honeycomb surface bands, for Fe ( $d_{xy}$ ,  $d_{x^2-y^2}$ ), ( $d_{xz}$ ,  $d_{yz}$ ), and triangular Ge  $p_z$  orbitals, respectively. A U-shaped band centered at  $\Gamma$  at about -0.3 eV is observed at the honeycomb surface which mainly comes from ( $d_{xz}$ ,  $d_{yz}$ ) of Fe. This band agrees with ARPES results. (e)-(h): same as (a)-(d) but for the kagome surface. The definition of the two surface terminations is given in Fig. S5.

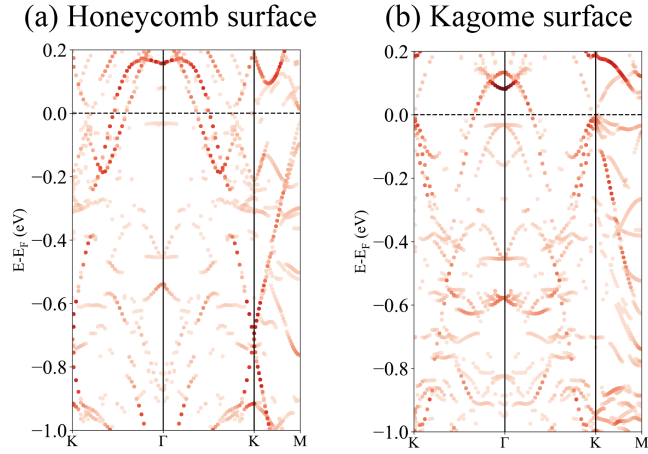


FIG. S14. The unfolded surface bands in the CDW phase, for both honeycomb surface (a) and kagome surface (b).

## S7. DIFFUSE SCATTERING, DS

Single crystal's diffuse scattering contains information about local (short-range, pairs of sites) ordering in the sample and the deviations from the average (different types of disorder), and gives information at scales beyond the average unit cell. In this section, we present a comprehensive study of the different DS cuts of as-grown FeGe, annealed and Ge-deficient FeGe and FeSn.

First of all, we will give a brief introduction about how to identify substitutional from displacement (phonon driven) disorder [18]. A system with substitutional disorder can be characterized by a unit cell where a site is occupied by one of several atom types or a missing atom, thus the chemical environment in neighbouring unit cells is not identical. Figure S15 (A) and (B) shows an example of a one dimensional substitutional disordered chain with a random occupation per unit cell and two different types of atom types; i.e. Fe and Ge. If Fe and Ge are present in a fraction  $m_{\text{Fe}}$  and  $m_{\text{Ge}}$ , respectively, then:

$$m_{\text{Fe}} + m_{\text{Ge}} = 1, \quad (\text{S1})$$

In a system with positive correlated disorder, Fe and Ge coherently cluster together; e.g. neighboring atoms are of the same type, figure S15 (A). If disorder is negatively correlated if Fe and Ge alternate along the chain, e.g. Fe tends to have Ge as its neighbor, figure S15 (B). Starting from a toy model, a binary disordered system is commonly characterized by the Warren-Cowley short-range order parameters  $\alpha_{\vec{v}}$ :

$$\alpha_{\vec{v}} = 1 - \frac{P_{\vec{v}}^{\text{FeGe}}}{m_{\text{Fe}}m_{\text{Ge}}}, \quad (\text{S2})$$

-where  $P_{\vec{v}}^{\text{FeGe}}$  describes the probability to find a Ge atom from a Fe atom at a vector  $\vec{v}$ . The positive and negative correlations in a certain direction are, thus, parametrized by Warren-Cowley short-range order values.

$$\alpha_{\vec{v}} = \begin{cases} > 0 & \text{positive correlation,} \\ = 0 & \text{no correlation,} \\ < 0 & \text{negative correlation.} \end{cases} \quad (\text{S3})$$

The Warren-Cowley parameters are equivalent to the interaction energies obtained by DFT in the main text.

The diffraction patterns for a positive, negative and uncorrelated one dimensional lattice are displayed in figure S15 (C). The main observation is a decrease of intensity as a function of the momentum transfer. Moreover, positive correlation gives large diffraction intensity at integer values of  $h$ , while a negative  $\alpha_{\vec{v}}$  localizes the intensity at half-integer  $h$  (in between Bragg peaks).

In a system with pure displacement disorder the atoms are displaced from their average position within the unit cell. This is the case for thermal disorder or the condensation of a particular phonon mode associated with a CDW phase transition. Therefore, it is strongly dependent on the phonon eigenvectors and polarization and the electron-phonon interaction. The displacement vector of an atom in a unit cell  $t$  on site  $i$  from its average position is given by  $\vec{\delta}_{t,i}$  and follows a Gaussian probability with a covariance matrix  $\underline{u}$ :

$$p(\vec{\delta}_{t,i}) = \frac{1}{\sqrt{(2\pi)^3 \det(\underline{u})}} \exp\left(-\frac{1}{2}(\vec{\delta}_{t,i})^T \underline{u}^{-1}(\vec{\delta}_{t,i})\right), \quad (\text{S4})$$

The displacement disorder is random if the displacement of an atom is independent of the displacement of its neighbouring sites, positively correlated if the displacement of neighbouring atoms is preferably along the same direction or along opposing directions (negative correlation). The diffuse diffraction pattern of a positive, a negative and an uncorrelated system driven by displacement disorder is shown in figure S16.

The signature of diffuse scattering caused by displacement disorder is a decrease of the maximum intensity at  $h \rightarrow 0$ , where the substitutional disorder develops its maximum intensity. Therefore, the momentum dependence of the diffuse scattering allows to directly distinguish between displacement and substitutional disorder. This is the case observed in FeGe, where the DS follows the typical trend characteristic of substitutional disorder instead of phonon-driven.

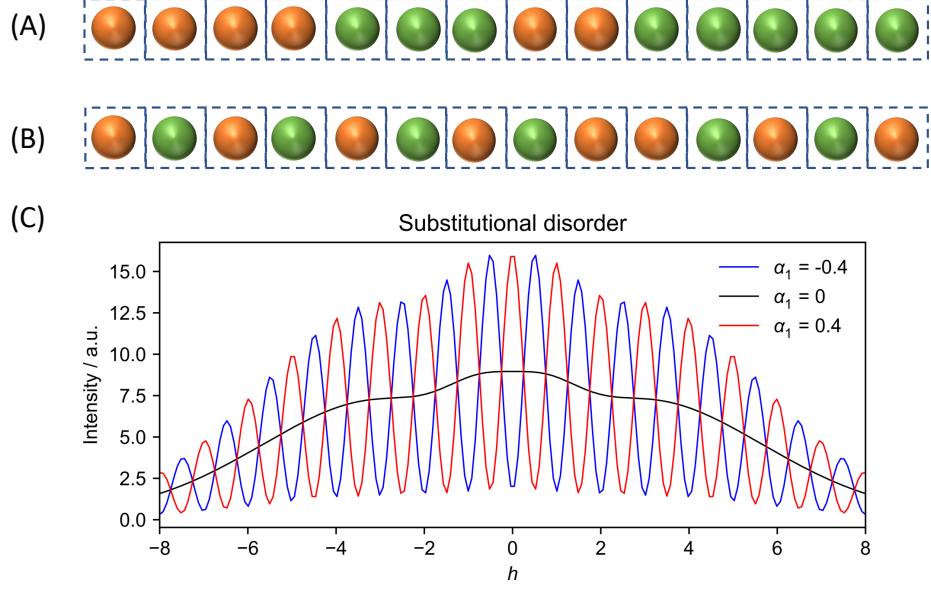


FIG. S15. (A) 1D-chain of Fe and Ge atoms with substitutional disorder, where (A) the same type of atoms (Fe or Ge) cluster together and (B) Fe and Ge type of atoms alternate in the chain. (C) Diffuse scattering pattern for substitutional disordered pattern. Note how the DS decreases with  $h$ .

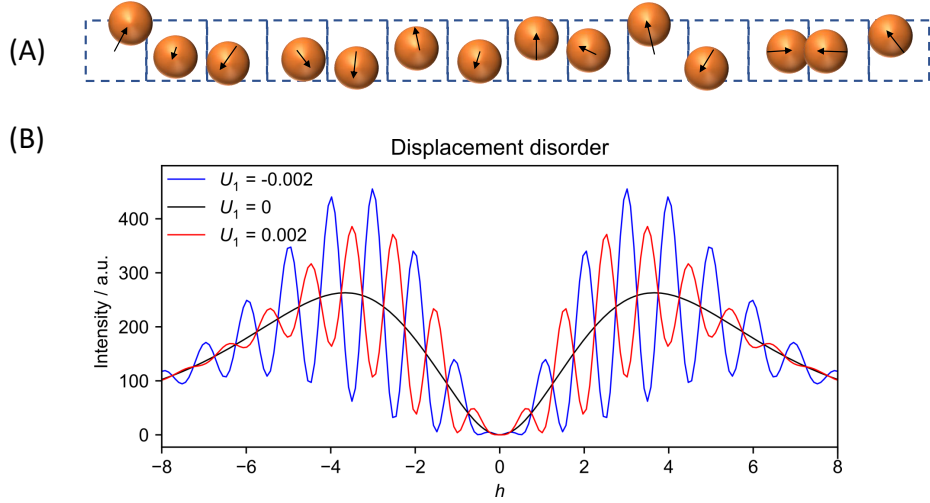


FIG. S16. (A) Diffuse scattering form a one-dimensional Ge crystal with displacement disorder. In (A), the arrows stand for the atomic displacements. (B) Calculated DS for correlated ( $U$  positive, atoms move in-phase) and uncorrelated ( $U$  negative, atoms move out-of-phase). The DS is negligible at  $h \rightarrow 0$ , hence differentiating from the substitutional disorder case. Note that positive correlation give maxima of DS at the Bragg positions, while negative correlation gives DS at half-integer  $h$ .

### A. FeGe

In figure S17 (A-C), we show the  $(h k)$  DS cuts for  $L=3, 1.5$  and  $2.5$  planes. Signatures of DS driven by substitutional disorder, namely hexagonal diffuse rings, are also visible at the  $(h k 3)$  plane. Similarly to the  $(h k 1.5)$  plane, the  $(h k 2.5)$  shows a complex diffuse pattern, presumably as a result of the small in-plane atomic displacements not considered in the MC simulations.

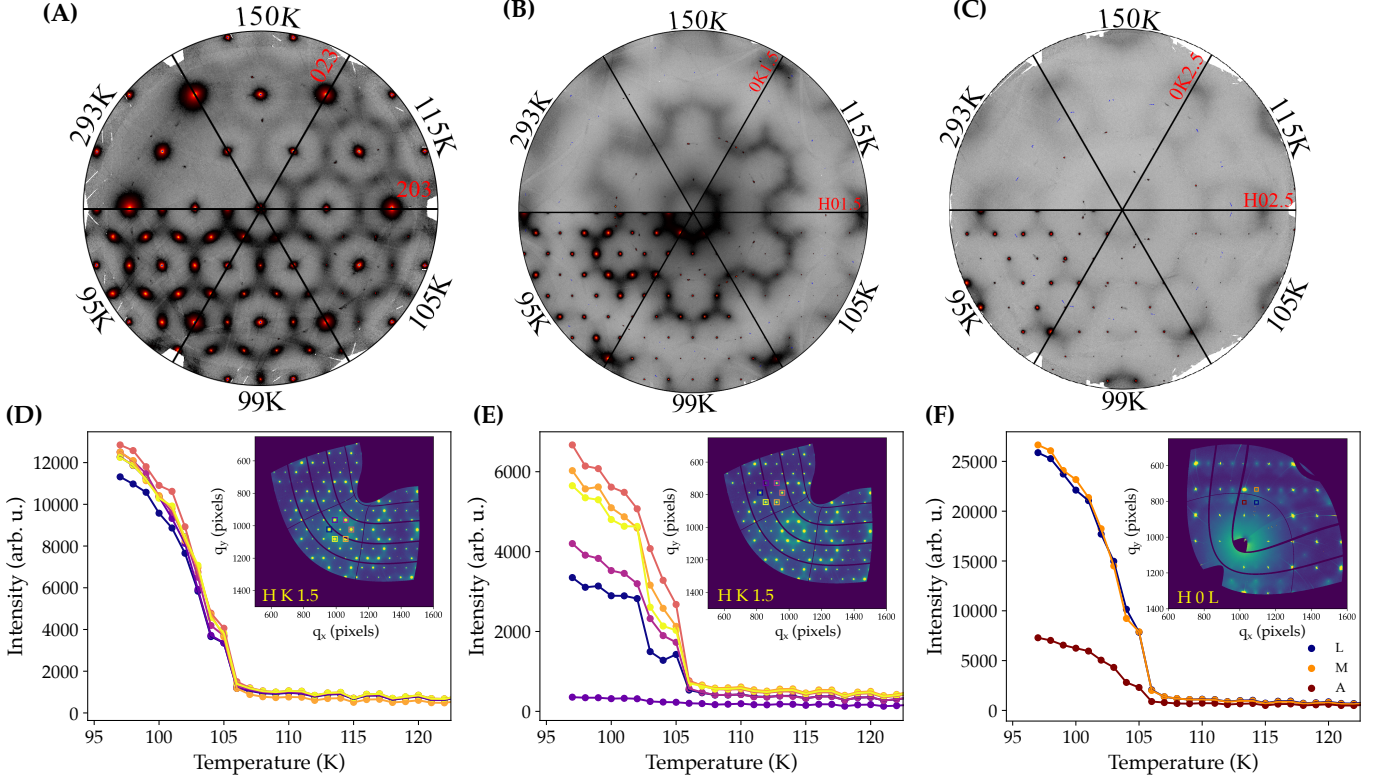


FIG. S17. DS maps of FeGe and integrated intensities of CDW peaks. (A) DS map of  $(h k 3)$ . (B) DS map of  $(h k 1.5)$ . (C) DS map of  $(h k 2.5)$ . (D) Temperature evolution of the integrated intensities of the CDW peaks around the position  $(0 0 1.5)$ . (E) Temperature evolution of the integrated intensities of the CDW peaks around the position  $(2 0 1.5)$ . (F) Temperature evolution of the integrated intensities of the CDW peaks at A, M and L in the  $h 0 l$  plane. In the inset of the panels (D-F), the squares are the integrated areas for each plot.

Figures S17 (D-F) display the integrated intensity of the CDW peaks and the corresponding diffuse precursors defined by the region of interest (ROI) in the insets. The intensities are strongly modulated in reciprocal space surrounding the Bragg points.

### B. Annealed FeGe

As-grown single crystals of FeGe (hereafter FeGe(a)) were annealed for 3 days at 300°C to increase the CDW correlation length [19]. The spatial correlation of the CDW extends to  $30.0 \pm 0.7$  nm along M,  $33.9 \pm 0.6$  nm along L and  $43.3 \pm 0.6$  nm along A. As we can see in figure S18 (A), the diffuse scattering, although with less signal to background ratio, is again localized along the M-L directions and also develops a hexagonal pattern at  $T > T_{CDW}$ .

Furthermore, at integer L and half integer L-values, streaks of diffuse intensity, characteristic of orthorhombic domains, are visible between Bragg peaks. On the other hand, the hexagonal diffuse pattern is no longer visible at low temperature, suggesting that the annealing reduces the frustration between dimerized and undimerized phases at  $T < T_{CDW}$ .

Figure S19 compares the  $(h k 2)$  DS of the annealed and as-grown FeGe. Three features are clearly visible: (1) the DS of the as-grown samples present larger signal-to-noise ratio, (2) streaks of diffuse intensity appear in between Bragg peaks and cross the CDW DS at M and (3) the as-grown CDW peak width is more anisotropic than the annealed FeGe. We note that due to the lower intensity of the DS of FeGe(a) and the presence of orthorhombic domains precludes us to reach a reliable comparison the anisotropic width ratio between FeGe(a) and as-grown crystals.

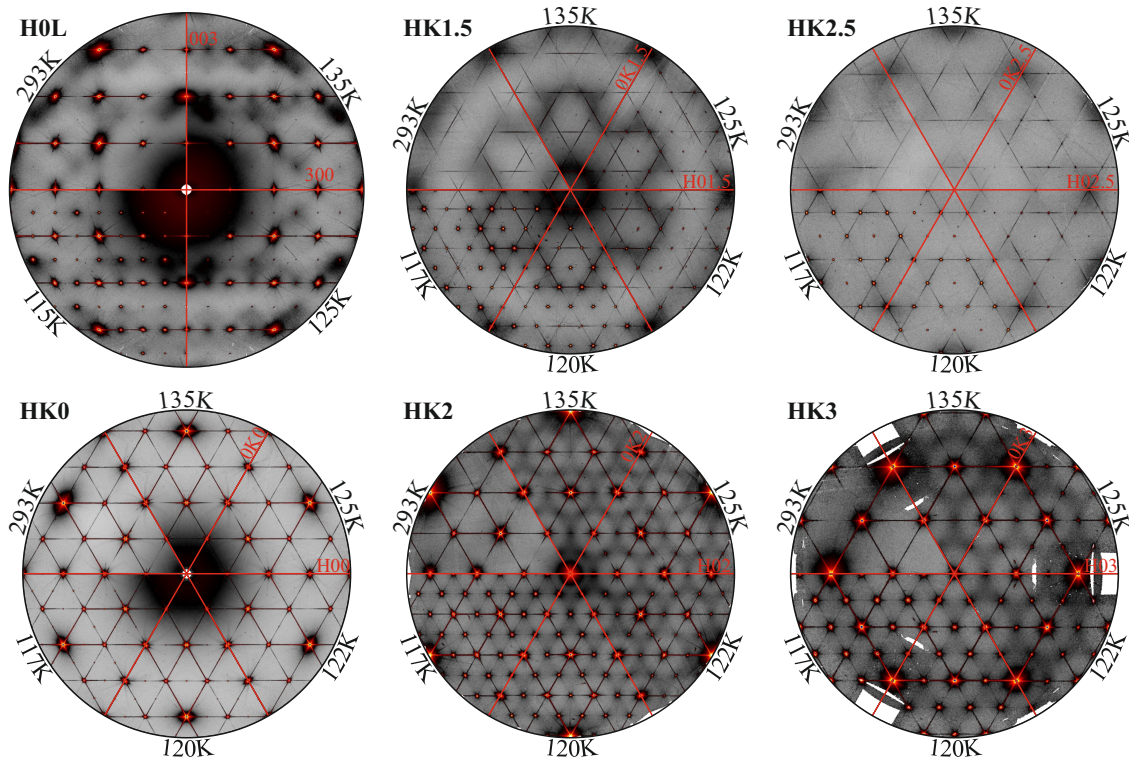


FIG. S18. DS maps of the annealed FeGe. The hexagonal diffuse rings are still present at  $T > T_{CDW}$  but, nevertheless, absent for  $T < T_{CDW}$ . In addition, no anisotropic DS is observed at the M point.

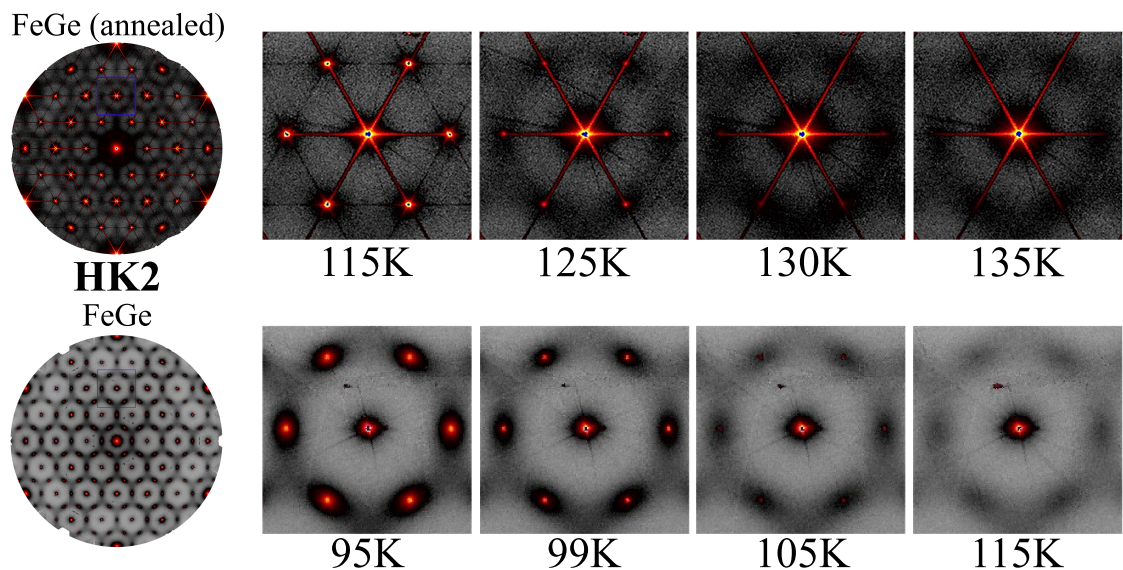


FIG. S19. Comparison of the (h k 2) annealed (A) and as-grown (B) FeGe crystals. (A) The DS of the annealed sample is at the background level and the diffuse signal is isotropic around the CDW reflection.

### C. $\text{FeGe}_{0.9}$

In this section, we present the results of Ge-deficient  $\text{FeGe}$  ( $\text{FeGe}_{0.9}$ ). The Ge concentration was estimated from the energy dispersive analysis (EDX), figure S20. The 10% Ge deficiency slightly modifies the magnetic behavior of the sample, but the CDW and the AFM canting transition are still visible, figure S21.

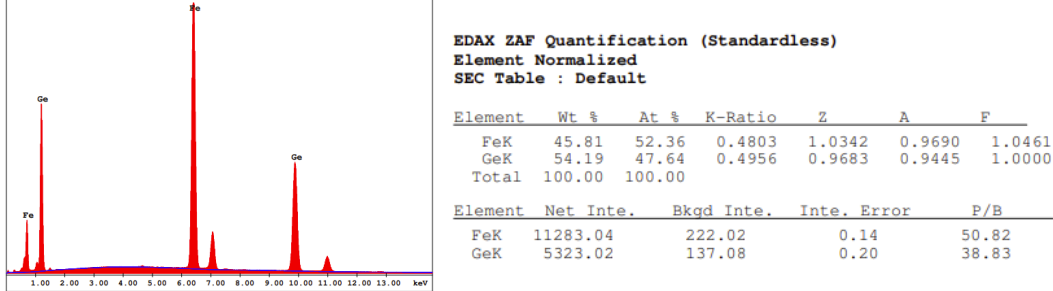


FIG. S20. Energy dispersive analysis of Ge-deficient  $\text{FeGe}$  ( $\text{FeGe}_{0.9}$ ).

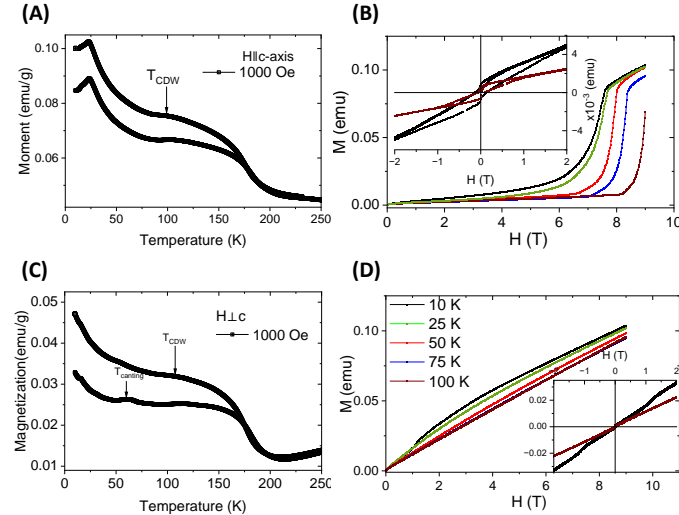


FIG. S21. Magnetic characterization of Ge-deficient  $\text{FeGe}$  (A) Temperature dependence of the magnetization for applied magnetic field ( $H$ ) parallel to the  $c$ -axis (B) Magnetic field dependence of the magnetization for  $H$  parallel to  $c$ . Temperature (C) and magnetic field (D) dependence of the magnetization parallel to the  $ab$ -plane.

The DS maps of  $\text{FeGe}_{0.9}$  show similar hexagonal diffuse patterns at integer and half integer  $L$ -values as the stoichiometric  $\text{FeGe}$ . However, the intensity of the CDW peaks sharply drops below the  $T_{\text{CDW}}$ , see figure S22, with an upturn for some propagation vectors and even the complete disappearance of the CDW reflection at  $q_A = (0\ 0\ \frac{3}{2})$ . This behavior was not observed in  $\text{FeGe}_{1.0}$ . We have carried out energy resolved inelastic x-ray scattering (XS) experiments to disentangle the elastic and inelastic contributions of the diffuse signal. As shown in figure S23, the drop of intensity is mostly driven by the temperature dependence of the elastic central peak (CP) of the IXS spectrum.

The temperature dependence of the CP, and in particular the absence of the elastic signal at  $(0\ 0\ \frac{3}{2})$  at low temperature, is reminiscent to the reports charge ordered nickelates [20]. Although not explored in detail, we speculate with the role of quenched disorder or fluctuating charge order below  $T_{\text{CDW}}$  that may hint at a competition between CDW and magnetism.

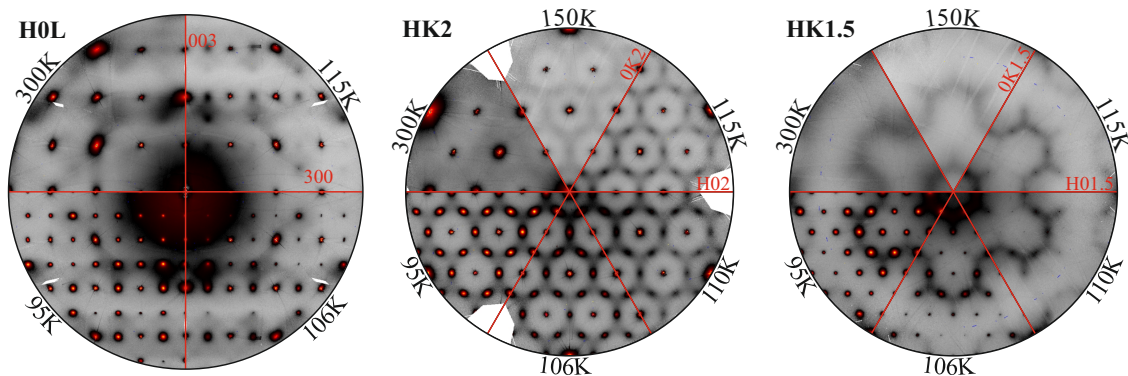


FIG. S22. Reciprocal space reconstructions of the Ge-deficient FeGe<sub>0.9</sub> diffuse maps.

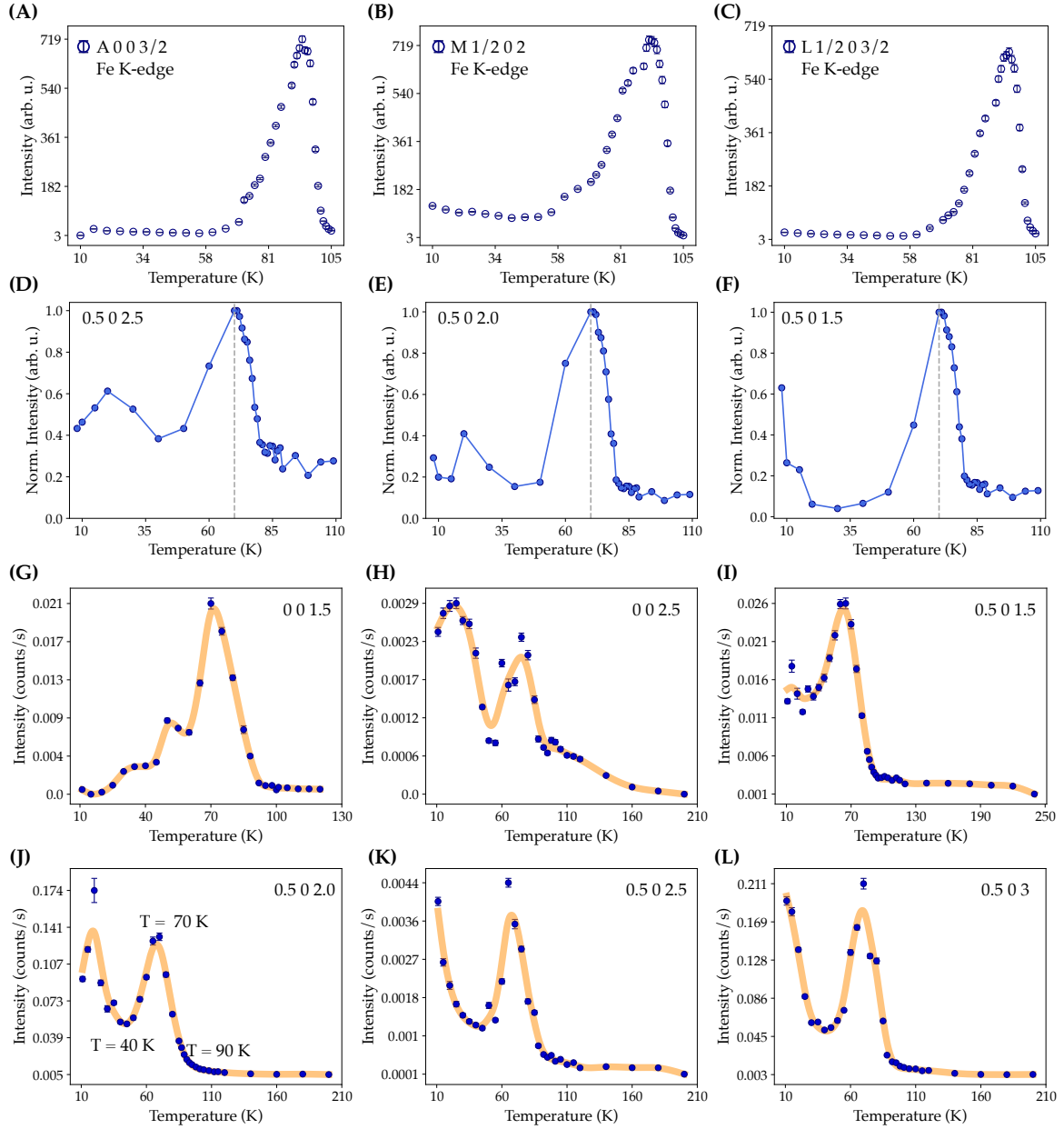


FIG. S23. (A-C) Temperature dependence of the CDW peaks A, M and L, respectively, measured at the Fe K-edge, 7.11 keV. (D-F) Temperature dependence of the DS integrated intensity of three different CDW peaks. (G-L) Temperature dependence of the integrated intensity of the elastic central peak (CP) of IXS for the Ge-deficient  $\text{FeGe}_{0.9}$ .

#### D. FeSn

We have searched for diffuse scattering in the antiferromagnetic FeSn with the in-plane spin polarization [21]. The absence of any type of diffuse pattern as a function of temperature demonstrates that the out-of-plane spin polarization of FeGe is responsible for the out-of-plane displacement of the trigonal Ge.

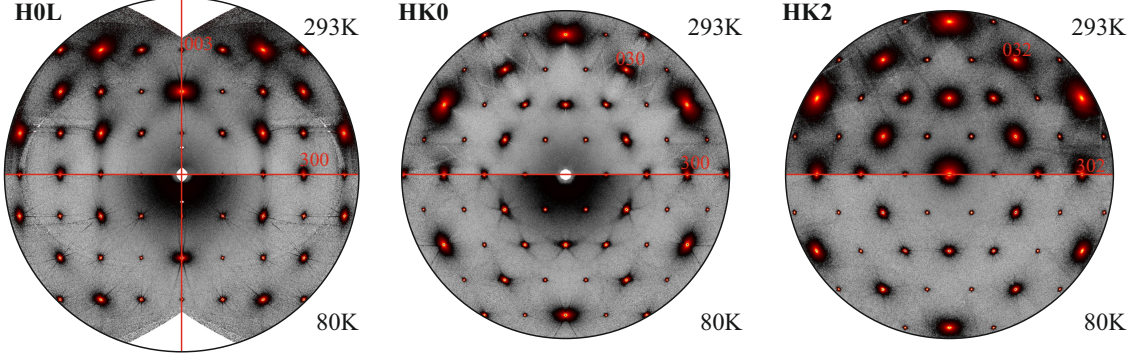


FIG. S24. Temperature dependence DS of FeSn. No diffuse signal is observed at either M, L or A points.

The DS around the Bragg peaks at high temperature is a result of the thermal excitations of phonons; i.e. thermal diffuse scattering (TDS).

## S8. MONTE CARLO SIMULATION OF DS

In this section, we use Monte Carlo to simulate the DS based on an effective Ising model that describes the dimerization of triangular Ge.

### A. Ising model for Ge dimerization

We first build an Ising model to describe the dimerization of triangular Ge and to achieve a certain microscopic realisation via the Monte Carlo simulations. We use an Ising variable  $\sigma_i = \pm 1$  to denote the dimerized ( $\sigma_i = -1$ ) and undimerized ( $\sigma_i = +1$ ) triangular Ge pair in the (non-CDW AFM phase) unit cell  $\mathbf{R}_i$ . By considering in-plane nearest neighbor (NN) coupling  $c_1$ , next NN (NNN) coupling  $c_2$ , 3rd-NN (3NN) coupling  $c_3$ ,  $z$ -direction NN coupling  $c_4$ , and an effective magnetic field  $h$ , we build a model with the form

$$H = \sum_{\langle ij \rangle:NN} c_1 \sigma_i \sigma_j + \sum_{\langle ij \rangle:NNN} c_2 \sigma_i \sigma_j + \sum_{\langle ij \rangle:3NN} c_3 \sigma_i \sigma_j + \sum_{\langle ij \rangle:z-NN} c_4 \sigma_i \sigma_j + \sum_i h \sigma_i + E_0. \quad (\text{S5})$$

where  $E_0$  is a constant and  $\langle ij \rangle$  means each  $ij$  pair counts only once. The magnetic field term  $h$  is added because the fully dimerized and undimerized configurations have different energies.

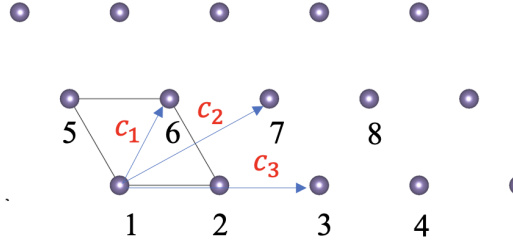


FIG. S25. The illustration of the coupling parameters used in the effective Ising model in Eq. (S5). In the figure,  $c_{1,2,3}$  are in-plane NN, NNN, and 3NN coupling parameters. The numbers 1-8 label the eight Ge pairs in a  $4 \times 2$  in-plane supercell of the non-CDW unit cell. The black lines mark the non-CDW unit cell.

We then fit the parameters from DFT. We choose a  $4 \times 2 \times 2$  supercell of the non-CDW AFM unit cell, which contains  $4 \times 2 \times 2$  Ge pairs. As shown in table S3, we consider 7 inequivalent dimer configurations and compute their averaged magnetic moments and total energies in DFT. The parameters in the Ising model Eq. (S5) are fitted using the DFT data, with their values summarized in table S4.

Dimer configuration	$\bar{\mu}_{Fe}/\mu_B$	DFT total energy (meV)	Fitted energy (meV)
$-+ -+, ++ +, -+ -, ++ +$	1.44	0.0	0.0
$++ +, ++ +, ++ +, ++ +$	1.39	835.4249	772.5727
$-+ +, -+ +, -+ +, -+ +$	1.44	997.3268	997.3268
$-+ +, ++ -, -+ +, ++ -$	1.43	667.4307	667.4307
$-+ +, ++ +, -+ +, ++ +$	1.41	517.8678	517.8678
$-+ -, ++ +, ++ +, ++ +$	1.41	614.8985	740.6027
$-+ -, ++ +, ++ +, +- -$	1.44	771.4848	708.6327

TABLE S3. The computed total energies from DFT for different dimer configurations. For each dimer configuration, + (−) denotes the dimerized (undimerized) triangular Ge pair. The first 8 ± denotes the 8 Ge pairs marked in Fig. S25 on the first layer in the  $4 \times 2 \times 2$  supercell, and the second 8 ± denotes the second layer. The second column of  $\bar{\mu}_{Fe}$  is the averaged magnitude of magnetic moment on Fe atoms. The third column is the computed DFT total energy, while the last column is the fitted energy using Eq. (S5). Remark that the configurations with more dimerized Ge have larger magnetic moments and much higher total energies, and are not used in the fitting.

### B. Monte Carlo simulation

With the effective Ising model derived based on DFT, we perform Monte Carlo simulations to obtain simulated diffuse scattering patterns. In the Monte Carlo simulation, moves are accepted if a random number (0-1) is less than  $\exp(-\Delta E/k_B T)$  with

$c_1$	$c_2$	$c_3$	$c_4$	$h$	$E_0$
45.885	25.267	-8.224	-44.290	-330.340	3746.100

TABLE S4. The fitted value of parameters in the Ising model Eq. (S5) based on the *ab initio* data in table S3. All numbers are given in meV.

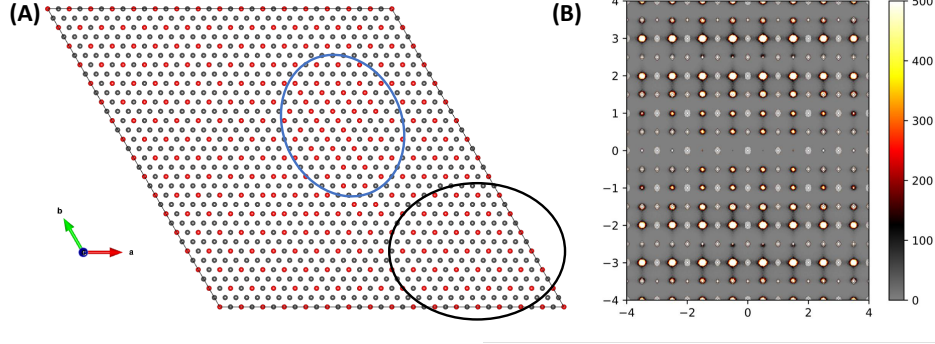


FIG. S26. (A) Converged MC simulation of a supercell of FeGe using the Ising model defined in S5. The circles highlight the 2 typical atomic arrangement. (B)  $(h \ 0 \ l)$  calculated DS map of FeGe showing the diffuse signal at the A, M and L points. Bragg peaks are omitted.

$T = 80K$ . The low-temperature unit cell ( $10 \times 10 \times 8 \text{ \AA}$ ) was expanded to a  $16 \times 16 \times 16$  supercell.  $\sim 5\%$  dimers were added randomly and the MC simulations were run until convergence.

The real space configuration of the minimum energy supercell is depicted in Fig. S26,(A) where the red and grey balls stand for dimerized and non-dimerized phases. Most of the atoms are highly ordered (circled in black) but there are some defect areas where the ordering is not complete (circled in blue). These configurations converged to 37.5% non-dimers and 62.5% dimers.

The diffuse scattering calculated from these configurations using DFT parameters (Bragg peaks have been removed) is plotted in figures S26 (B) and S27 (A). The diffuse scattering is calculated using the program Scatty by Fourier transforming of all the atomic coordinates of the atomic positions. In figure S27 (A-F), the high intense Bragg nodes at the A point are removed.

The DFT values reproduce the DS at the M and L points, figure S27 (A-B). Moreover, upon manually tuning the  $c_1$  and  $c_2$  values, we can also simulate the shape of the anisotropic DS at the M point at 80 K and 100 K. This shows that the  $c_i$ 's parameters that describe the nearest neighbour interaction between dimerized and undimerized trigonal Ge are temperature dependent.

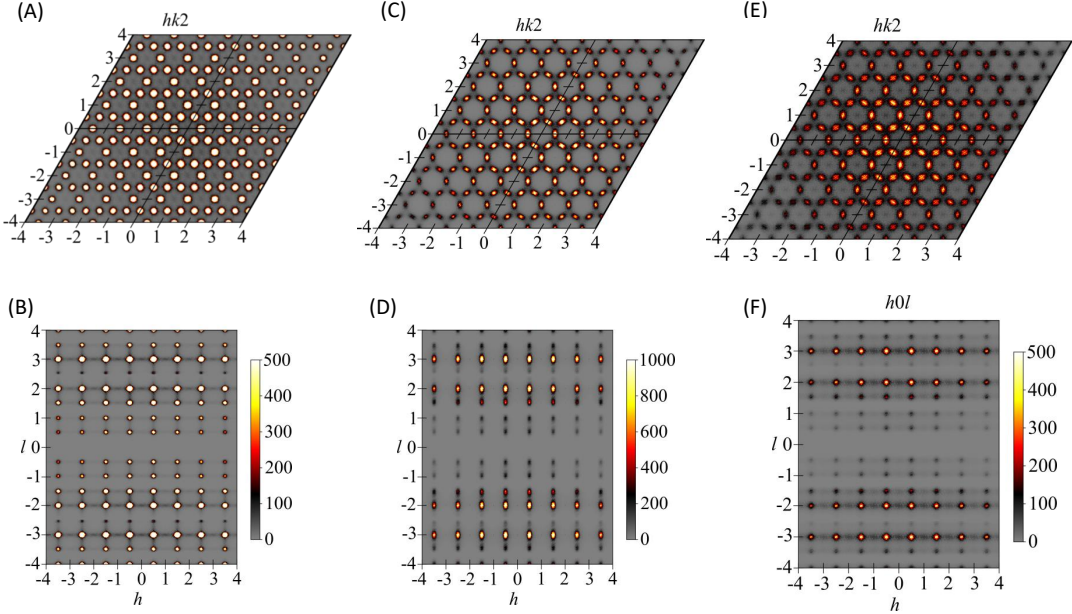


FIG. S27. Simulated  $h k 2$  and  $h 0 L$  DS maps. (A-B)  $h k 2$  and  $h 0 1$  DS obtained by minimising the Ising hamiltonian using the  $c_i$  values obtained from DFT,  $c_1 = 45.885$  meV,  $c_2 = 25.267$  meV,  $c_3 = -8.224$  meV,  $c_4 = -44.290$  meV,  $h = -330.340$  meV (T=80 K). (C-D)  $h k 2$  and  $h 0 1$  DS for  $c_1 = 165.886$  meV,  $c_2 = 25.267$  meV,  $c_3 = -8.224$  meV,  $c_4 = -44.290$  meV (T=80 K). (E-F)  $h k 2$  and  $h 0 1$  DS  $c_1 = 165.886$  meV,  $c_2 = 0$  meV,  $c_3 = -8.224$  meV,  $c_4 = -44.290$  meV (T=100 K). The simulations do not include the in-plane atomic displacements, which are responsible for the absence of DS at  $l=\text{integer}+\frac{1}{2}$ . See main text.

## S9. BOND-ORDER CORRELATION FUNCTION ANALYSIS

In this section, we describe the analysis of the bond-order correlation function analysis. For a discrete set of particles in the real-space, one can define a local ordering between nearest neighbors as

$$\Psi_6(\mathbf{r}_k) = \frac{1}{N_k} \sum_{j=1}^{N_k} e^{i6\theta_{kj}}, \quad (\text{S6})$$

where  $N_k$  is the number of nearest neighbors of the  $k$ -particle at position  $\mathbf{r}_k$  and  $\theta_{kj}$  defines the angle the  $k$ - $j$  bond (fig. 4(I) in the main text). For a particle at  $\mathbf{r}_k$ , the six-bond order correlation function at a distance  $|\mathbf{r} - \mathbf{r}_k|$  is given by

$$G_6(|\mathbf{r} - \mathbf{r}_k|) = \frac{1}{N_{|\mathbf{r} - \mathbf{r}_k|}} \sum_j^{N_{|\mathbf{r} - \mathbf{r}_k|}} \Psi_6(\mathbf{r}_k) \Psi_6^*(\mathbf{r}_j), \quad (\text{S7})$$

where the sum goes over all the particle at a distance  $|\mathbf{r} - \mathbf{r}_k|$  with respect to  $\mathbf{r}_k$ . Summing over all the particles in the system, we can define a total  $G_6(\mathbf{r})$ ,

$$G_6(\mathbf{r}) = \frac{1}{N_r} \sum_{<j,k>}^{N_r} \Psi_6(\mathbf{r}_k) \Psi_6^*(\mathbf{r}_j), \quad (\text{S8})$$

- where  $N_r$  goes over any pair of particles which are at a distance  $r$ . To compute the  $G_6(\mathbf{r})$  correlation function, first we need to get the real-space charge distribution from the diffuse scattering maps. The intensity  $I$  of a diffuse scattering map is proportional to the square of the structure factor,

$$I \propto |S(\mathbf{q})|^2, \quad (\text{S9})$$

- where  $\mathbf{q}$  is a vector in the reciprocal space. The real-space charge distribution is defined as the real part of the Fourier transform of the structure factor,

$$\rho(\mathbf{r}) = \frac{1}{V_{\text{cell}}} \sum_{\mathbf{q}}^N |S(\mathbf{q})| \cos(2\pi(\mathbf{q} \cdot \mathbf{r}) + \Phi(\mathbf{q})), \quad (\text{S10})$$

- where  $\mathbf{r}$  is the position vector in the real space and  $\Phi(\mathbf{q})$  is a random phase  $S(\mathbf{q})$  for a given  $\mathbf{q}$  [22–24].

As Eq. S8 is defined over a discrete set of particles, we make a discretization of the continuous real-space charge distributions by defining the local maxima as particles. Then, we introduce a Voronoi tessellation in the discrete set of particles to define the concept of neighbor. Given a set of points (particle's positions)  $\{p_1, p_2, \dots, p_N\}$ , each point  $p_i$  has a Voronoi cell associated. This cell consists in any point in the Euclidean space for which  $p_i$  is the nearest site of the set of points. All the Voronoi cells together form the Voronoi tessellation and any pair of cells which share a boundary will correspond to a pair of points which are neighbors. The geometrical construction of this diagram is equivalent to the one used to get a Wigner-Seitz cell. Once we have introduced the concept of neighbor in the discrete set of particles, we can compute Eqs. S6, S7, S8.

Figure S28 summarizes the real space charge density considering different types of CDW peak shape/anisotropy for a 6-fold symmetry. In figure S28 (A,C,E), where the CDW peaks are rather sharp, we can discretize the charge density to perform a Voronoi analysis, however, at high temperature as is the case of figure S28 (I), the transformation from a continuous field to a discrete set of particles, where there is no well-defined six-fold symmetry, the charge density is well capture by means of a discretization analysis. Figure S29 (A,D,G,J) correspond to the experimental maps of diffuse scattering we have used to perform the  $G_6$  analysis in the Figure 4 of main text. For each one of these DS we have performed the Fourier transform to real space (see Figure (B,E,H,K)) via Eq. S10. After the discretization, we got the Voronoi tessellation and made the bond-order correlation function via Eq. S8.

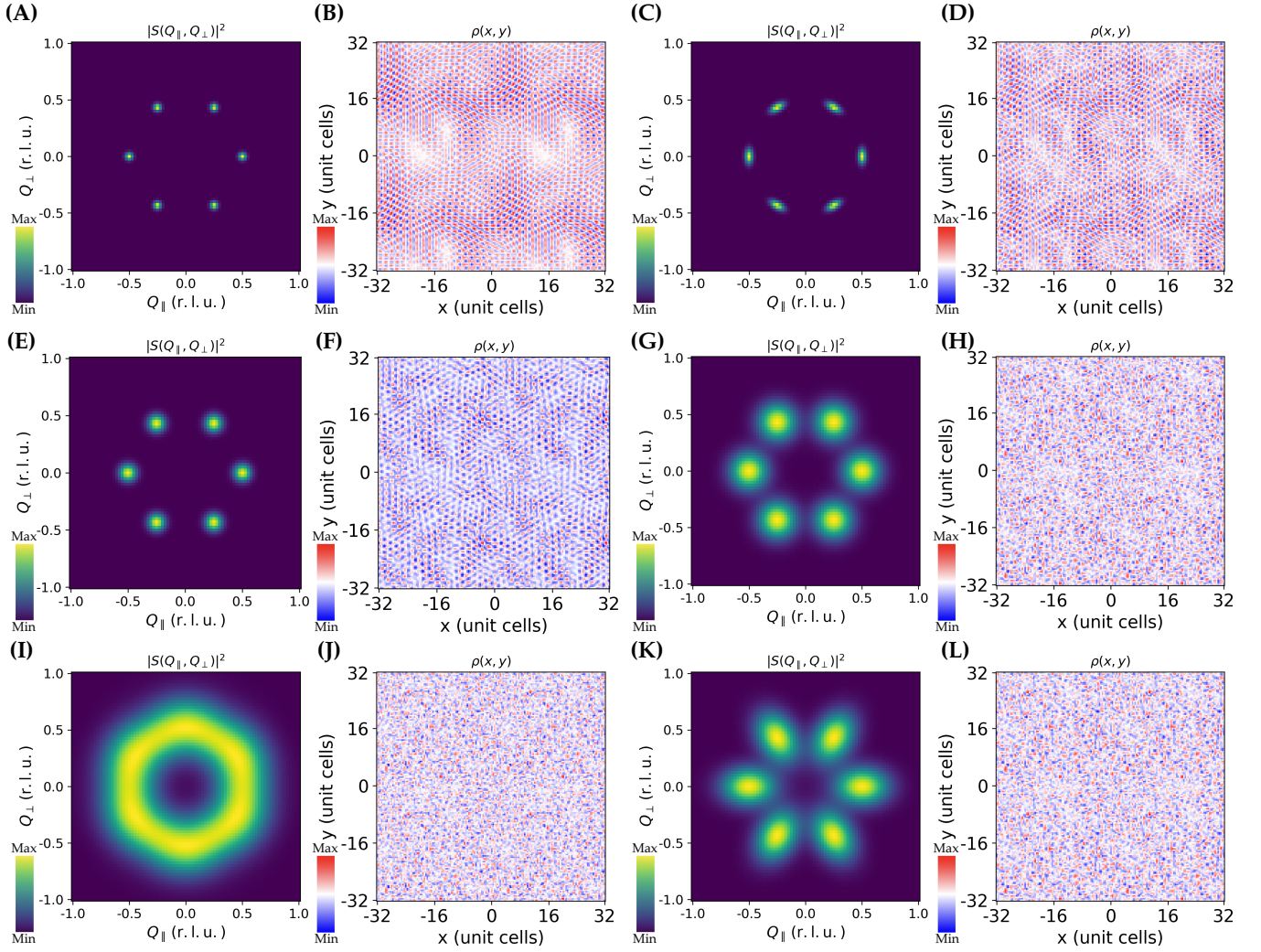


FIG. S28. (A) Simulated DS map by using a Gaussian Lineshape centered at each CDW peak and linewidths  $[\sigma_x, \sigma_y]$  equal to  $[0.002, 0.002]$  r.l.u.. (B) Fourier transform of (A). Each pair from (C-L) are the same varying the linewidths of the Gaussians. (C-D) DS and its Fourier transform where the Gaussians have a linewidth of  $[0.01, 0.002]$  r.l.u.. (E-F) DS and its Fourier transform where the Gaussians have a linewidth of  $[0.01, 0.01]$  r.l.u.. (G-H) DS and its Fourier transform where the Gaussians have a linewidth of  $[0.05, 0.05]$  r.l.u.. (I-J) DS and its Fourier transform where the Gaussians have a linewidth of  $[0.3, 0.3]$  r.l.u.. (K-L) DS and its Fourier transform where the Gaussians have a linewidth of  $[0.05, 0.1]$  r.l.u.. For each Fourier transform it was used the same random phase matrix.

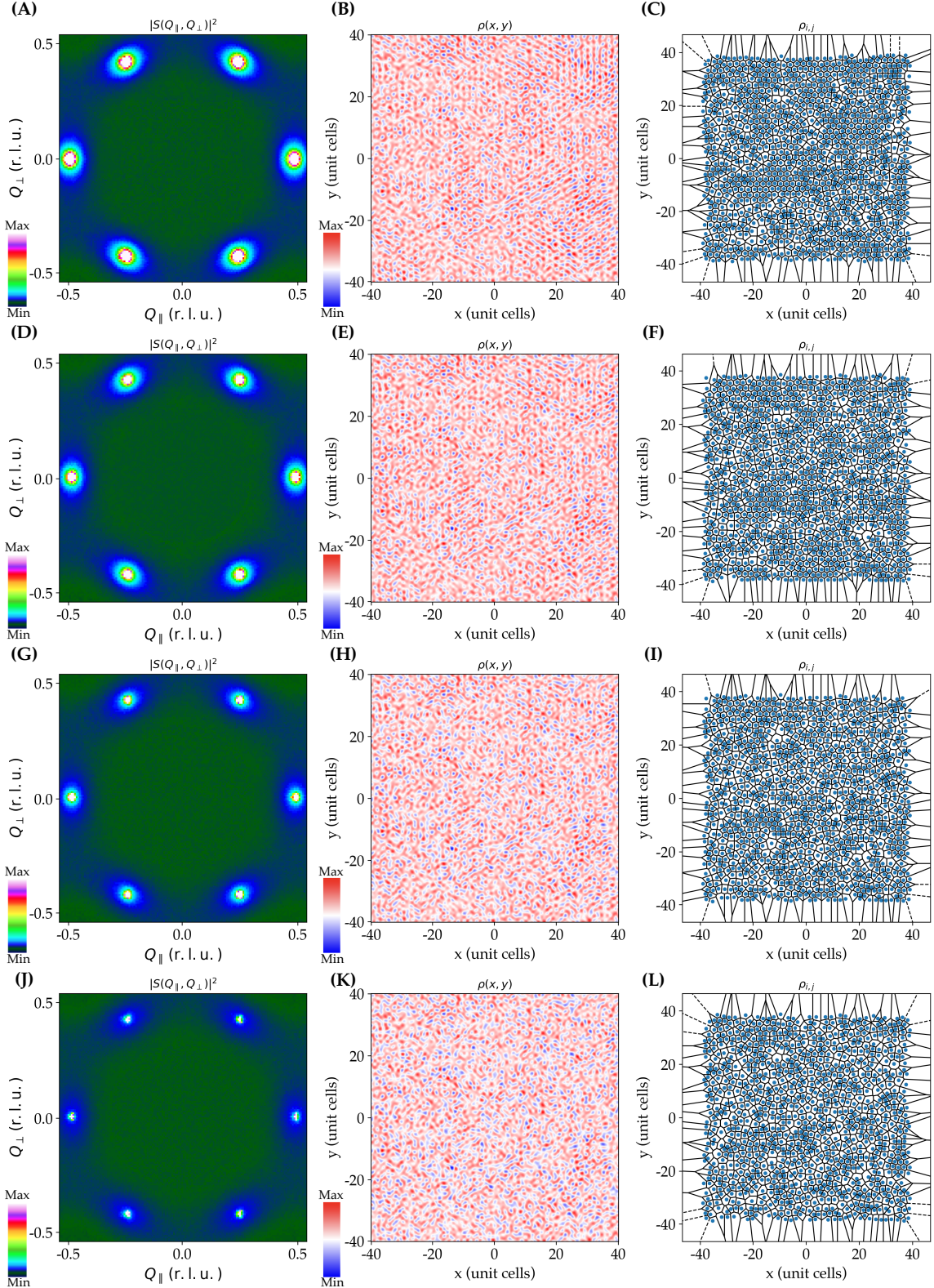


FIG. S29. (A,D,G,J) Diffuse Scattering maps of the plane (H K 2.0) around the point (0 0 2.0) for  $T = 95, 97, 99, 101$  K, respectively. The Bragg point just in the point (0 0 2.0) has been screened by introducing random Gaussian noise with and average and standard deviation equal to the thermal background. (B,E,H,K) Real-space charge distribution for the diffuse scattering maps of (A,D,G,J), respectively. (C,F,I,L) Voronoi tessellation of the local maxima of the charge distribution in (B,E,H,K), respectively.

---

[1] Xiaokun Teng, Lebing Chen, Feng Ye, Elliott Rosenberg, Zhaoyu Liu, Jia-Xin Yin, Yu-Xiao Jiang, Ji Seop Oh, M. Zahid Hasan, Kelly J. Neubauer, Bin Gao, Yaofeng Xie, Makoto Hashimoto, Donghui Lu, Chris Jozwiak, Aaron Bostwick, Eli Rotenberg, Robert J. Birgeneau, Jiun-Haw Chu, Ming Yi, and Pengcheng Dai, "Discovery of charge density wave in a kagome lattice antiferromagnet," *Nature* **609**, 490–495 (2022).

[2] Xiaokun Teng, Ji Seop Oh, Hengxin Tan, Lebing Chen, Jianwei Huang, Bin Gao, Jia-Xin Yin, Jiun-Haw Chu, Makoto Hashimoto, Donghui Lu, Chris Jozwiak, Aaron Bostwick, Eli Rotenberg, Garrett E. Granroth, Binghai Yan, Robert J. Birgeneau, Pengcheng Dai, and Ming Yi, "Magnetism and charge density wave order in kagome FeGe," *Nature Physics* **19**, 814–822 (2023).

[3] Georg Kresse and Jürgen Furthmüller, "Efficiency of ab-initio total energy calculations for metals and semiconductors using a plane-wave basis set," *Computational materials science* **6**, 15–50 (1996).

[4] Georg Kresse and JPRB Hafner, "Ab initio molecular dynamics for open-shell transition metals," *Physical Review B* **48**, 13115 (1993).

[5] Georg Kresse and Jürgen Hafner, "Ab initio molecular dynamics for liquid metals," *Physical review B* **47**, 558 (1993).

[6] Georg Kresse and Jürgen Hafner, "Ab initio molecular-dynamics simulation of the liquid-metal–amorphous-semiconductor transition in germanium," *Physical Review B* **49**, 14251 (1994).

[7] Georg Kresse and Jürgen Furthmüller, "Efficient iterative schemes for ab initio total-energy calculations using a plane-wave basis set," *Physical review B* **54**, 11169 (1996).

[8] John P Perdew, Kieron Burke, and Matthias Ernzerhof, "Generalized gradient approximation made simple," *Physical review letters* **77**, 3865 (1996).

[9] Nicola Marzari and David Vanderbilt, "Maximally localized generalized wannier functions for composite energy bands," *Physical review B* **56**, 12847 (1997).

[10] Ivo Souza, Nicola Marzari, and David Vanderbilt, "Maximally localized wannier functions for entangled energy bands," *Physical Review B* **65**, 035109 (2001).

[11] Nicola Marzari, Arash A Mostofi, Jonathan R Yates, Ivo Souza, and David Vanderbilt, "Maximally localized wannier functions: Theory and applications," *Reviews of Modern Physics* **84**, 1419 (2012).

[12] Giovanni Pizzi, Valerio Vitale, Ryotaro Arita, Stefan Blügel, Frank Freimuth, Guillaume Géranton, Marco Gibertini, Dominik Gresch, Charles Johnson, Takashi Koretsune, et al., "Wannier90 as a community code: new features and applications," *Journal of Physics: Condensed Matter* **32**, 165902 (2020).

[13] Yi Jiang, Haoyu Hu, Dumitru Călugăru, Claudia Felser, Santiago Blanco-Canosa, Hongming Weng, Yuanfeng Xu, and B Andrei Bernevig, "Kagome materials ii: Sg 191: FeGe as a lego building block for the entire 1: 6: 6 series: hidden d-orbital decoupling of flat band sectors, effective models and interaction hamiltonians," *arXiv preprint arXiv:2311.09290* (2023).

[14] QuanSheng Wu, ShengNan Zhang, Hai-Feng Song, Matthias Troyer, and Alexey A Soluyanov, "Wanniertools: An open-source software package for novel topological materials," *Computer Physics Communications* **224**, 405–416 (2018).

[15] Q Zheng, "Vasp band unfolding," URL <https://github.com/QijingZheng/VaspBandUnfolding> (2018).

[16] Voicu Popescu and Alex Zunger, "Extracting e versus k effective band structure from supercell calculations on alloys and impurities," *Physical Review B* **85**, 085201 (2012).

[17] Mitsuaki Kawamura, "Fermisurfer: Fermi-surface viewer providing multiple representation schemes," *Computer Physics Communications* **239**, 197–203 (2019).

[18] T.R. Welberry, *Diffuse X-Ray Scattering and Models of Disorder*, IUCr monographs on crystallography (Oxford University Press, 2022).

[19] Xueliang Wu, Xinrun Mi, Long Zhang, Chin-Wei Wang, Nour Marayta, Xiaoyuan Zhou, Mingquan He, Michael Merz, Yisheng Chai, and Aifeng Wang, "Annealing-tunable charge density wave in the kagome antiferromagnet fege," (2024), [arXiv:2308.01291](https://arxiv.org/abs/2308.01291).

[20] Alessandro Ricci, Nicola Poccia, Gaetano Campi, Shravan Mishra, Leonard Müller, Boby Joseph, Bo Shi, Alexey Zozulya, Marcel Buchholz, Christoph Trabant, James C. T. Lee, Jens Viefhaus, Jeroen B. Goedkoop, Agustinus Agung Nugroho, Markus Braden, Sujoy Roy, Michael Sprung, and Christian Schüßler-Langeheine, "Measurement of spin dynamics in a layered nickelate using x-ray photon correlation spectroscopy: Evidence for intrinsic destabilization of incommensurate stripes at low temperatures," *Phys. Rev. Lett.* **127**, 057001 (2021).

[21] Ming Kang, Jonathan Pelliciari, Alex Frano, Nicholas Breznay, Enrico Schierle, Eugen Weschke, Ronny Sutarto, Feizhou He, Padraic Shafer, Elke Arenholz, Mo Chen, Keto Zhang, Alejandro Ruiz, Zeyu Hao, Sylvia Lewin, James Analytis, Yoshiharu Krockenberger, Hideki Yamamoto, Tanmoy Das, and Riccardo Comin, "Evolution of charge order topology across a magnetic phase transition in cuprate superconductors," *Nature Physics* **15**, 335–340 (2019).

[22] R. Comin, R. Sutarto, E. H. da Silva Neto, L. Chauviere, R. Liang, W. N. Hardy, D. A. Bonn, F. He, G. A. Sawatzky, and A. Damascelli, "Broken translational and rotational symmetry via charge stripe order in underdoped  $\text{YBa}_2\text{Cu}_3\text{O}_{6+y}$ ," *Science* **347**, 1335–1339 (2015).

[23] B. V. Fine, "Comment on 'broken translational and rotational symmetry via charge stripe order in underdoped  $\text{YBa}_2\text{Cu}_3\text{O}_{6+y}$ ,'" *Science* **351**, 235–235 (2016).

[24] R. Comin, R. Sutarto, E. H. da Silva Neto, L. Chauviere, R. Liang, W. N. Hardy, D. A. Bonn, F. He, G. A. Sawatzky, and A. Damascelli, "Response to comment on 'broken translational and rotational symmetry via charge stripe order in underdoped  $\text{YBa}_2\text{Cu}_3\text{O}_{6+y}$ ,'" *Science* **351**, 235–235 (2016).